Crystallographic control and texture inheritance during mylonitization of coarse grained quartz veins

Alberto Ceccato[1*], Giorgio Pennacchioni[1], Luca Menegon[2], Michel Bestmann[3]

[1] Department of Geosciences, University of Padova, Via Gradenigo 6, I-35131 Padova, Italy

[2] School of Geography, Earth and Environmental Sciences, Plymouth University, United Kingdom

[3] GeoZentrum Nordbayern, Friedrich-Alexander-Universität Erlangen-Nürnberg (FAU), Germany

* Corresponding author.

Tel.: +39 0498279106; fax: +39 049 8279134

E-mail: alberto.ceccato.2@phd.unipd.it

Abstract

Quartz veins within Rieserferner pluton underwent deformation during post-magmatic cooling at temperature close to 450 °C. Different crystallographic orientations of cm-sized quartz vein crystals conditioned the evolution of microstructures and crystallographic preferred orientations (CPO) during vein-parallel simple shear up to high shear strains ($\gamma \approx 10$). For $\gamma < 2$, crystals stretched to ribbons of variable aspect ratios. The highest aspect ratios resulted from {m}<a> glide in ribbons with c-axis sub-parallel to the shear zone vorticity Y-axis. Ribbons with c-axis orthogonal to Y (XZ-type ribbons) were stronger and hardened more quickly: they show lower aspect ratios and fine (grain size ~ 10-20 μm) recrystallization along sets of microshear zones (μSZs) exploiting crystallographic planes. Distortion of XZ-type ribbons and recrystallization exploit preferentially those slip systems with misorientation axis close to Y. New grains of μSZs initiated by subgrain rotation recrystallization (SGR) and thereupon achieved high angle misorientations by a concurrent process of heterogeneous rigid grain rotation around Y associated with the confined shear within the μSZ. Dauphiné twinning occurred pervasively, but did not played a dominant role on μSZ nucleation. Ribbon recrystallization became widespread at $\gamma > 2$ and pervasive at $\gamma \approx 10$. Ultramylonitic quartz veins are fine grained (~ 10 μm, similar to new grains of μSZ) and show a

CPO banding resulting in a bulk c-axis CPO with a Y-maximum, as part of a single girdle about orthogonal to the foliation, and orientations at the pole figure periphery at moderate to high angle to the foliation. This bulk CPO derives from steady-state SGR associated with preferential activity, in the different CPO bands, of slip systems generating subgrain boundaries with misorientation axes close to Y. The CPO of individual recrystallized bands is largely inherited from original crystallographic orientation of the ribbons (and therefore vein crystals) from which they derived. High strain and pervasive recrystallization were not enough to reset the initial crystallographic heterogeneity and this CPO memory is explained by a dominance of SGR. This contrast with experimental observation of a rapid erasure of a pristine CPO by cannibalism from grains with the most favourably oriented slip system under dominant grain boundary migration recrystallization.

1. Introduction

Quartz is one of the most representative minerals of continental crust rocks and has been commonly assumed to control the first-order rheology of large portions of the ductile crust (e.g. Ranalli, 2000). This explains the huge effort made in understanding quartz rheology during geological deformation. Physical deformation experiments have determined constitutive flow laws for quartz under different laboratory conditions (e.g., Luan and Paterson, 1992; Hirth and Tullis, 1992; Gleason and Tullis, 1995; Hirth et al., 2001). Application of these lab-determined flow laws to natural deformation implies extrapolation to over several orders of magnitude in strain rate (from < 10^{-5} s^{-1} to values as high as 10^{-12}-10^{-16} s^{-1}) and the reliability of such extrapolation is legitimized by the similarity of microstructures, crystallographic preferred orientations (CPO) and inferred recrystallization mechanisms between the experimentally and naturally deformed quartz (e.g. Hirth et al., 2001; Mancktelow and Pennacchioni, 2010). With this aim numerous experimental studies have investigated the development and evolution of microstructures and CPO with strain (Tullis et al., 1973; Tullis, 1977; Dell'Angelo and Tullis, 1989; Gleason et al., 1993; Heilbronner and Tullis, 2006; Muto et al., 2011). Due to limitations of experimental apparatus, deformation experiments on quartz have been conducted on either single quartz crystals (Hobbs, 1968; Vernooij et al., 2006a, b;

Muto et al., 2011) or on relatively fine-grained natural and synthetic quartz aggregates (e.g.: novaculite, Black Hill quartzite). The experiments on quartz single crystals are of particular relevance for the interpretation of many natural mylonitic quartz where recrystallized aggregates were derived from coarse original grains (several mm to tens of mm in grain size); either quartz grains of granitoid rocks and metamorphic rocks (Kilian et al., 2011; Bestmann and Pennacchioni, 2015) or quartz crystals from veins (Stipp et al., 2002; Pennacchioni et al, 2010; Price et al., 2016). The experiments of Muto et al. (2011) have evidenced a control of the initial quartz crystallographic orientation with respect to the imposed stress field on the crystal strength, recrystallization rate and developing CPO of recrystallized aggregates. However, Muto et al. (2011) observed that all crystals developed, during dynamic recrystallization, distinct domains with a CPO consistent with the favoured {m}<a> slip that rapidly cannibalized the aggregates with other unfavourable orientations with increasing shear. The memory of the original crystallographic orientations was totally erased after a relatively small amount of shear. This experimental result is not consistent with the observed evolution of some mylonitic quartz veins that shows a more long-lasting heredity of the original crystallographic orientations of parent grains in the CPO of recrystallized aggregates (Pennacchioni et al., 2010).

We present here the analysis of the microstructural and CPO evolution at increasing strain of quartz veins from a simple geological setting of a cooling pluton, similar to the context described in Pennacchioni et al. (2010). This analysis reveals a complex evolution over large strain determined by the initially different orientations of the vein crystals. This initial heterogeneity in crystal orientations is not dismantled by mylonitization up to stages of complete dynamic recrystallization.

2. Geological background and field description

The 32 Ma old Rieserferner pluton (Eastern Alps) (Romer and Siegesmund, 2003) belongs to a series of intrusions emplaced along the Periadriatic Lineament in the Eocene-Oligocene (referred to as Periadriatic magmatism: Rosenberg, 2004). This pluton, emplaced at a depth of 12-15 km (0.25-0.35 GPa: Cesare, 1994) into the Austroalpine tectonic unit, consists of 3 main granitoid intrusions of coarse-grained garnet-bearing tonalites, granodiorites and fine-grained leucogranites (Bellieni, 1978; Steenken et al., 2000; Wagner et al., 2006). The estimated cooling time of the pluton to equilibrate to the ambient temperature varies between 1.5 and 2 Ma, depending on the cooling model and the reference host rock temperature (350 °C: Steenken et al., 2000; 425 °C: Wagner et al., 2006). During post-magmatic cooling the intrusive rocks were deformed along ductile shear zones and cataclastic faults that overprinted the variably developed sub-magmatic to solid-state foliations associated with both the emplacement-related doming process (Wagner et al., 2006) and the activity of the Defereggen-Antholz-Vals tectonic line (Mancktelow et al., 2001). The ductile shear zones, typically few centimetres in thickness, exploited precursor joints and joint-filling veins, as it is commonly observed in other granitoid plutons (e.g. Adamello: Pennacchioni, 2005; Sierra Nevada: Pennacchioni and Zucchi, 2013) and in meta-granitoid units (Mancktelow and Pennacchioni, 2005; Pennacchioni and Mancktelow, 2007; Menegon and Pennacchioni, 2010).

Quartz veins of variable thickness (up to few decimetres thick) occurs along a shallowly ESE-dipping joint set (mean dip-direction/dip: N115°/20°), that almost invariably localized top-to-E normal ductile shearing at conditions close to 450°C and 0.3 GPa (results from thermodynamic modelling not reported in this paper). Deformed veins, ranging from protomylonites to ultramylonites, have been sampled for the study presented here (Figs. 1a-c). The protomylonites are coarse grained (reflecting the multi-millimetric grain size of the pristine quartz vein crystals) and show an oblique rough foliation forming an angle in the range between 20° and 30° to the vein boundary (Fig. 1a). The ultramylonites are fine grained, with a macroscopic flinty aspect, and show a pervasive foliation oriented at a very low angle to the vein boundary (Fig. 1c).

3. Microstructure of deformed quartz veins

In the kinematic reference system adopted here for the shear zones, the X axis is parallel to the stretching direction, the XY plane is parallel to the vein boundary, and the Z direction is orthogonal to the vein boundary. Thin sections were cut parallel to the XZ plane. The microstructure and the CPO of quartz in deformed quartz veins were analysed by: polarized light microscopy, computer integrated polarization microscopy (CIP) and electron backscattered diffraction (EBSD). CIP allowed the expeditious microstructure-linked analysis of the c-axis orientations of the coarse grained protomylonites over large thin section areas (mm^2 to cm^2). The details of the CIP and EBSD methods are given in the Appendix. Assuming simple shear within the tabular-shaped quartz veins, the shear strain γ localized into the vein was estimated from the angle θ between the internal oblique foliation and vein boundary according to the equation (Ramsay, 1980):

$$\tan 2\theta = -2/\gamma$$

3.1 Protomylonitic quartz veins

3.1.1. Ribbon grains

Weakly deformed quartz veins (Figs. 1a, 2a and, in supplementary online material, SOM1a) are characterized by largely predominant monocrystalline quartz ribbons, with different crystallographic orientation, which define a foliation inclined 20-30° to the vein boundary. Shear strains γ of 1.3 and 2.1 were estimated for the 2 analysed protomylonite samples.

The cumulative results of the microstructural analysis of 2 thin sections are shown in Fig. 2 (thin sections shown in Figs. 2a and SOM1a). In Figs. 2b and SOM1b, the different quartz ribbons are colour-coded, based on the CIP analysis, as a function of their dominant c-axis orientation according to the look-up-table of Figs. 2c and SOM1d. The cumulative c-axis CPO of the ribbons from the 2 thin sections shows a clustering (i) along a girdle approximately orthogonal to the ribbon elongation, and (ii) along the pole figure periphery, with a main clustering of the c-axes at a high angle to the ribbon elongation (Figs. 2c and SOM1d). We observe a difference in the ribbon microstructure depending on the c-axis orientation allowing the distinction of 3 end-member types: (1) Y-type ribbons, with c-axis close to Y (Fig. 3a); (2) Z-type ribbons, with c-axis close to Z (Fig. 3b); (3) XZ-type ribbons, with c-axis plotting along the pole figure periphery in intermediate position between X and Z. The XZ-type ribbons can be further distinguished in XZa- and XZb-types with the c-axis almost orthogonal and parallel to the ribbon elongation, respectively (Figs. 3c-f).

The aspect ratio of ribbons is shown, for the different ribbon c-axis orientations, in the pole figure of Fig. 2d. The measured aspect ratios are minimum values, given that most of the ribbons exceed in length the thin section width, but there is a clear relationship between the measured aspect ratios and the c-axis orientations (Fig. 2d): (i) the lowest aspect ratios (as low as about 2) belong to XZ-type ribbons, and especially to XZa-types; and (ii) most of the high aspect ratios (as high as 17.5) belong to Y-type ribbons.

3.1.2. Recrystallization of ribbons

The quartz ribbons of protomylonites show incipient recrystallization to fine-grained aggregates that are distinguished with a black colour in the microstructural sketches of Figs. 2b and SOM1b. On average over the whole thin section, the recrystallized aggregates form about 10% of the area. The new grains have an average grain size, determined from EBSD data (see Appendix for the methods), between 10 and 20 µm. Figure 2e shows the area fraction of recrystallized aggregates for to the different c-axis orientations of the host ribbons and indicates that recrystallization is larger (as much as 23% of ribbon area) in Z- and XZ-type ribbons. In Y-type ribbons, the recrystallization is very limited or absent. The different crystallographic orientations of the ribbons also translate into a difference of the internal deformation microstructures and of the geometry of the recrystallized aggregates:

1) Y-type ribbons show subgrains elongated parallel to the ribbon elongation, sweeping undulose extinction and limited recrystallization preferentially located at the ribbon boundaries (Fig. 3a).

2) Z-type ribbons show weak undulose extinction, a single set of deformation lamellae (fine extinction bands, FEB: Derez et al., 2015) and recrystallized aggregates scattered across the ribbon or arranged along sharp discontinuities aligned sub-parallel to the ribbon elongation (Fig. 3b). In the most deformed ribbons (or portions of ribbons), recrystallized aggregates are clustered into elongated domains, inclined at variable angle with respect to the ribbon elongation, locally forming

intersecting sets (lower ribbon portion in Fig. 3b). Coarse (100's of μm in size) polygonization and recrystallization resemble the blocky localized extinction bands described in Derez et al. (2015) (Fig. 3b).

3) XZ-type ribbons typically show bands of recrystallization arranged in two intersecting sets (Figs. 3c-f). These bands of recrystallization commonly correspond to micro-shear zones (μSZs) as inferred from the displacement of the orthogonal set of μSZs. The dominant set of μSZs is commonly oriented sub-parallel to the vein boundary. The other set is oriented at a high angle to the vein boundary, sub-parallel to Z or slightly rotated consistently with the shear sense (i.e. clockwise in all the images presented here showing dextral sense of shear: Figs. 4 and SOM1c). The direction of the μSZs are slightly different in different ribbons (Figs. 4 and SOM1c). The μSZs of each set have roughly a regular spacing (in the range between 10's of μm to 300 μm) on a local (sub-millimetric) scale, but the spacing and the spatial density are variable across the ribbon. On a local scale, the μSZs of both sets show a comparable thickness. The thickness of the μSZs correlates with the amount of accommodated slip (Fig. SOM2).

The XZa-type ribbons are almost free of an optically visible internal distortion (except for a weak undulose extinction) in between incipient μSZs (Fig. 3c). The domains cut by the μSZs preserve a roughly square-lozenge shape up to relatively high degree of ribbon recrystallization. The XZb-type ribbons commonly show a strong internal distortion manifested by undulose extinction and wide extinction bands (WEBs of Derez et al., 2015; e.g. outlined by white arrows in Fig. 3f) (Fig. 3d). The recrystallization aggregates of both XZa- and XZb-type have a strong CPO (evaluated with the gypsum plate) different from that of the host ribbon (e.g. Fig. 3c). In XZa-type ribbons, the position of c-axis of the recrystallized aggregates in pole plots is orthogonal to the boundary of the μSZs (Figs. 3c-e; “c-normal” shear bands of van Daalen et al., 1999). In XZb-type ribbons, the position of c-axis of the aggregates is almost parallel in pole plots, or slightly rotated with the sense of shear, to the boundary of the μSZs (Figs. 3d-3f; “c-parallel” shear bands of van Daalen et al., 1999). The CPO within the μSZs has been investigated in more detail by EBSD (see below).

3.1.3 Distribution of fluid inclusions

In protomylonites, fluid inclusions are mainly present within recrystallized aggregates, along the μSZ selvages and associated with polygonized domains of ribbons. In the latter case, subgrains are locally outlined by fluid inclusions. In secondary electrons SEM images on broken surfaces (Figs. SOM3a-b), the grain boundaries of recrystallized grains commonly show regularly arranged pores with crystallographically-controlled etch-pit type shapes (Mancktelow and Pennacchioni, 2004). Within relatively undeformed portions of XZ- and Z-type ribbons, local fluid inclusions are scattered and not arranged in trails. Y-type ribbons are mainly free of fluid inclusions. Recrystallized aggregates next to the μSZs, commonly decorated with fluid inclusions, contain locally small mica flakes that are aligned to define an internal foliation (Figs. SOM 3c-d).

3.2. Mylonitic quartz veins

Mylonitic quartz veins show a layered microstructure (Fig. 5a) determined by the alternation of: (i) high aspect ratio (>7) monocrystalline ribbons; (ii) partially recrystallized ribbons; and (iii) completely recrystallized layers. The amount of bulk recrystallization is close to 50% of the area. The grain size of the recrystallized grains is comparable with the one along the μSZ within the ribbons of the protomylonites. Shear strains γ of 3.5 and 6.6 have been estimated for the mylonite samples.

The monocrystalline ribbons are coarsely polygonized with prevalent subgrain boundaries orthogonal to the ribbon elongation (Z-type ribbons). Ribbon recrystallization occurred at the boundaries and along sharp bands trending parallel to the ribbon elongation (especially in Z-type ribbons; e.g. Figs. 5a-b). The layers of partially recrystallized ribbons include lozenge-shaped to elliptical quartz ribbon porphyroclasts (mainly XZa-type) embedded in the aggregate of recrystallized grains (Fig. SOM3e). Completely recrystallized layers show an extinction banding parallel to the foliation.

The cumulative CIP-determined c-axis pole figure of the monocrystalline ribbons resembles a type-

I girdle dominated by a concentration of c-axes in two small circles around the foliation pole (Fig. 5c). The bulk pole figure of the pervasively recrystallized domains consists of a short girdle (low density of c-axis poles at the pole figure periphery) oriented at a high angle to the foliation (Fig. 5d).

3.3 Ultramylonitic quartz veins

Ultramylonites consist of a dominant (> 90% area) matrix of fine-grained (10-15 µm determined by EBSD; see below) recrystallized grains that includes isolated quartz porphyroclasts (ribbon porphyroclasts) and high aspect ratio (> 50) monocrystalline ribbons (Fig. 5e). The extinction banding of the mylonitic aggregate and the ribbon grains define a foliation oriented at a low (~5°) angle to the vein boundary yielding a shear strain $\gamma > 10$. The recrystallized grains show a shape preferred orientation defining a foliation oblique to the extinction banding and inclined consistently with the shear sense (Figs. SOM3g-h).

The ribbon porphyroclasts range in shape from lozenge- to lenticular- and fish-shaped and have an asymmetry with stair-stepping geometry climbing against the sense of shear (Figs. SOM3f-g-h). As inferred from CIP and optical (gypsum-plate inserted: Fig. SOM3d) analysis, all the porphyroclasts have a similar c-axis orientation, about orthogonal to the mylonitic foliation.The CIP-determined bulk CPO of the ultramylonite shows a strong maximum close to Y, which is part of a single girdle inclined with respect to Z consistently with the sense of shear (Fig. 5g). This bulk CPO, derived from layers with different CPO, has been investigated in detail by EBSD (see below).

5. EBSD analysis

The EBSD analysis (Figs. 6-10) was performed on selected microstructures of protomylonite and ultramylonite. Information of EBSD analytical conditions are reported in the Appendix A. In protomylonites, Y- and XZ-type ribbons, and the associated recrystallization aggregates along µSZs, were investigated as microstructural end-members of the ribbon evolution. In ultramylonite, we have investigated both the CPO banding of the pervasively recrystallized matrix and a ribbon porphyroclast that survived such high strains.

5.1 EBSD analysis of protomylonite

5.1.1. Y-type ribbon

The analysed Y-type ribbon (Fig. 6a) shows a c-axis distribution in pole figure forming a short girdle centred on the Y-axis and oriented orthogonal to the ribbon elongation (Fig. 6b). The subgrain boundaries are mostly straight and sub-parallel to the ribbon elongation with a spatial density increasing towards the zones of incipient recrystallization at the ribbon boundaries. The subgrains of highly polygonized domains and the few new grains have a similar grain size of about 15-20 μm. The misorientation angle distribution (MAD) (both correlated and uncorrelated) shows a strong maximum at low angle misorientations (< 20°) and, for correlated misorientations, at around 60° (Fig. 9a). In crystal coordinates, the low angle misorientation (< 15°) axes show higher density towards the c-axis and weakly around {m}; for high angle misorientations (close to 60°) there is a high density towards the c-axis (Fig. 6c). In sample coordinates, the low angle misorientation axes show high density close to the Y-axis (Fig. 6c) and at the pole figure periphery coinciding with {m} poles, and there is an overall distribution to define a girdle sub-parallel to the ribbon elongation. The high angle misorientations axes (mainly related to misorientations with angle ~ 60°: Fig. 10a) show high density around Y (i.e., sub-parallel to the c-axis) (Fig. 6c).

5.1.2. XZa- and XZb-type ribbons

The EBSD analysis was conducted on both XZa- (Figs. 7 and SOM6) and XZb-type ribbons (Fig. 8) and on included μSZs with different degrees of evolution: incipient (one to few grains thick), evolved (in the range between few grains and 100s μm thick), and mature (several 100s μm thick). The μSZs of XZa- and XZb-type ribbons are similar in their microstructural evolution and are described together.

5.1.2.1 Internal distortion of the host ribbons

Both XZa-type and XZb-type ribbons show a heterogeneous internal distortion (Figs. 7b and 8b) consistent with rotation of crystallographic directions around an axis sub-parallel to Y. This results in a dispersion along the periphery to over 45° of the c-axis orientations (Figs. 7b and 8b). In the XZa-type ribbon, the low-angle low misorientation boundaries are heterogeneously distributed, wavy and poorly interconnected. In the XZb-type ribbon, low angle boundaries are straight with sets sub-parallel to the trace of rhombohedral planes (low angle boundaries of areas (1) and (2) of Fig. 8a). The MAD (Figs. 10b-c) for both types of ribbons show two maxima at low angle misorientations (< 15°) and at around 60°, similar to what observed for the Y-type ribbon. In crystal coordinates, all the analysed portions of XZa- and XZb-type ribbons show, as a bulk, a widely scattered distribution across the entire plot of low angle misorientation axes, but with increasing density towards the positive and negative rhombs (see scheme of Fig. 6e for reference) and especially towards the c-axis. It is of note that the distribution maxima are weak in all cases. This bulk distribution probably masks a rather more heterogeneous distribution of misorientation axes as indicated by the plots for the areas 1 and 2 in Fig. 8f showing more distinct clustering towards the c-axis (area 1) and along a girdle between rhombohedral crystallographic planes {r} and {z} (area 2) (see scheme of Fig. 6e for reference). The analysis of more strongly deformed portions of the XZ-b type ribbon adjacent to the incipient μSZs α and β also indicates distinct local patterns of low angle misorientation axis in comparison to the rest of the host ribbon (Figs. SOM4a-b).

In sample coordinates, the misorientation axes of XZa-type ribbon are clustered at the periphery of the pole figure close to the c-axis orientations of the host ribbon (Fig. 7e) for both low and high angle misorientations. For XZb-type ribbons the bulk misorientation axes are: (i) strongly clustered off-axis in the between Y and X in a region including the direction of {r} and the c-axis for low angle misorientations; and (ii) sub-parallel to the host c-axis for high angle misorientation (basically of 60°).

5.1.2.2 Incipient μSZs

Incipient µSZs are defined by discontinuous linear arrays of one-grain-thick recrystallization aggregates in alternation with, and flanked by, discontinuous subgrains rows (e.g. Fig. 8a). The new grains have the same size (about 10-20 µm) as the surrounding subgrains (Figs. 7a-b and SOM5a). The contact area between the host and the incipient µSZs is defined by one-subgrain-thick zone. The µSZ traces are sub-parallel to the trace of rhombohedral crystallographic planes of the host ribbon (Figs. 8b-c). The c-axes of the new grains are distributed, in a rotational sense consistent with the µSZ sense of shear (e.g., sinistral for the µSZs α and β that are inclined more than 45° to the shear plane: Fig. 8), along the pole figure periphery. The spreading of these c-axis orientations ranges from orientations close to that of the host grain to almost orthogonal orientations (Fig. 8c). The axis distributions of new grains, together with the lattice distortion of the host grain, are consistent with rotations around Y (anticlockwise for the sinistral µSZs α and β and clockwise for the dextral µSZ ϕ, ε and δ). The host ribbon can be in direct contact with highly misoriented new grains even in one-grain-thick µSZs.

The misorientation analysis of low angle boundaries (misorientations in the range of 2-15°) in the host grain adjacent to incipient µSZs α and β (enclosed in the black polygons marked in Fig. 8a) shows misorientation axes clustering parallel to primary (<r> and <z>) or secondary (<π> and <π'>) rhombohedral directions (inverse pole figure of Fig. SOM4). In sample coordinates, these axes show a clustering that is close to the Y-axis (Fig. SOM4). The small number of new grains of incipient µSZs (that show subgrain boundaries anyway) does not allow a statistically meaningful analysis of the misorientation axes.

5.1.2.3 Evolved µSZs

Evolved µSZs consist of recrystallized aggregates with a thickness of a few grains (µSZs δ of Fig. 7a, and ϕ of Fig. 8a). A transition zone (< 100 µm in thickness) between host crystal and the µSZ aggregate is discontinuously present and includes a high spatial density of low- and high-angle boundaries, and relatively high lattice distortion gradients (~ 0.25-0.5 °/µm, point-to-point smallest misorientation angle). These transition zones alternate with domains where recrystallized grains are in sharp contact with a weakly distorted portion of host grain (Fig. 7a: µSZ δ). High spatial density of subgrain boundaries is observed at intersections and stepover domains between µSZs. The subgrains next to µSZs and the new grains have comparable mean grain size of 10-20 µm (Figs. SOM5b and 7c). The 2 analysed µSZs are sub-parallel to the trace of either one of the positive {r} or negative {z} rhombohedral crystallographic planes (µSZ δ: Fig. 7b) and to the {m} crystallographic plane (µSZ ϕ: Fig. 8b).

As for incipient µSZs, the c-axis of new grains of evolved µSZs within both XZa- and XZb-type ribbons are distributed in a rotational sense from the host orientation with rotation axis sub-parallel to Y (Figs. 7c and 8d). Recrystallized grains are polygonal to sub-rectangular in shape, which results in common triple and four-grain junctions, and show a strong shape preferred orientation inclined consistently with the shear sense of the µSZs. The grain size is homogeneous within a single µSZ, but can be slightly different (of few µm) in different µSZs (Figs. SOM5c). Pores are observed both at triple junctions and along the grain boundaries (Figs. SOM3a-b).

In relatively coarse (grain size >15 µm) and high aspect ratio (>3) new grains, the boundaries of local subgrains are mostly oriented orthogonal to grain elongation (e.g. Figs. 7a and 8a). However, recrystallized grains are dominantly strain-free (lattice distortion gradient <0.2 °/µm, point-to-point smallest misorientation angle). Though the number of data is very small, the misorientations axis related to these subgrain boundaries plot close to either rhombohedral (<r> and <z>) or peripheral (<m> and <a>) crystal axes when analysed individually. The MAD for the evolved µSZs is comparable to the MADs for the host ribbons, in the case of µSZ ϕ (Fig. 9g), but differs in µSZ δ (Fig. 9e) for the presence of a wide range of misorientation angles also including intermediate values between 10° and 60°. In sample coordinates the misorientation axis distribution for both low and high angle (15-45°) misorientations of both the evolved µSZ δ (Fig. 7f) and ϕ (Fig. 8g) shows a higher density spot eccentric to the Y-directions (in addition to the spot close to c-axis direction observed for high angle misorientations).

5.1.2.4 Mature μSZs

The 2 analysed mature μSZs belong to XZa-type ribbons (Figs. 7 and SOM6) and trend parallel to the trace of one {r} plane of the host ribbon (e.g., μSZ ε in Figs. 7a-b). An irregular, discontinuous contact zone (< 200 μm thick) is locally present between the host ribbon and the recrystallized aggregate of the μSZs that involves a higher distortion and spatial density of subgrains of the ribbon (Figs. 7a and SOM6a). The recrystallized aggregate of the μSZs includes, close to its boundaries, relatively coarse relics of the host ribbons that show a core-and-mantle transition to the recrystallized grains in the interior of the μSZs. The subgrains in the host transition zone and within clasts inside the μSZs have a comparable size (10-20 μm, e.g. Fig. SOM6d) as the new recrystallized grains of the μSZs.

Similar to incipient and evolved μSZs, the mature μSZs also show a CPO with crystallographic axes dispersed (with rotation axis parallel to Y) from the orientations of the host grain (Figs. 7d and SOM6e-g). In the thicker μSZs of Fig. SOM6a, there is still a dispersion of crystallographic axes around Y, but the c-axis maxima are also spread towards intermediate positions of the pole figure (3 columns on the left of Figs. SOM6e-g), that can be in part associated with the larger distortion (and therefore crystallographic dispersion) of the host grain (Fig. SOM6b). The different domains distinguished in the mature μSZ of Fig. SOM6a, show distinct CPO, though still mainly referable to different degrees of rotational spreading of crystallographic axes around Y from the host orientation. These domains likely represent coherent portion of the host grain, dissected during the incipient stage of the μSZ evolution (as can be seen in the host grain of Fig. SOM6e), which underwent rigid rotation before extensively recrystallized in the μSZ.

The MADs of both the analysed mature μSZs is comparable with those of the evolved μSZ δ (Figs. 9f and 9h) .

In crystal coordinates, the low angle misorientation axis distributions have very low maxima for all domains, with concentrations along girdles between {r} and {z} poles (e.g. domains ω and ψ) and between {m} and <a> directions (e.g. domains ξ and ψ) (Figs. 7g; Figs. SOM6e-g). In sample coordinates there are stronger maxima of low angle misorientation axis towards the centre of the pole figure (Y-axis) in all domains with a tendency to distribute along a girdle in domain ξ (Fig. 7g; Figs. SOM6e-g).

5.2 EBSD analysis of ultramylonite

5.2.1. Recrystallized matrix

The EBSD map of the ultramylonite in Fig. 10a includes a large portion of recrystallized matrix showing a CPO banding and a large ribbon porphyroclast.

The bulk c-axis pole figure (Fig. 10b) shows a girdle slightly inclined to the YZ plane, with the sense of shear, and a peripheral concentration fading progressively towards the foliation plane and therefore resembles the type of pole figure determined for the protomylonites and mylonites (Figs. 2c and 5c, respectively). This bulk pole figure results from the combination of distinct c-axis CPO characteristic of the different layers composing the ultramylonite microstructure and referable to 3 main types (Figs. 10c-f): (1) layers with a c-axis short girdle, orthogonal to foliation, centred on the Y-axis (Fig. 10e) and showing a dominant red colour in Fig. 10a (e.g. layer III); (2) layers with c-axis maxima concentrated, along the bulk girdle, at intermediate positions between Y and the pole figure periphery (referred to as "intermediate orientation": Fig. 10f; layer IV) and showing violet and purple colour in Fig. 11a; (3) layers with c-axis maxima towards the pole figure periphery (referred to as "peripheral orientation": Figs. 10c-d; layer I-II) and showing dominant blue and green colours in Fig. 10a (e.g. domain I-II). The layers with the dominant peripheral c-axis direction commonly contain grains with an intermediate orientation, but rarely grains with a Y-orientation. These layers also commonly include quartz porphyroclasts.

The MAD indicates the presence of a strong maximum for correlated misorientations at low angle misorientations (< 15°) and a weak one for misorientations around 60° (Fig. 9i) for the bulk microstructure and also for the individual layers with distinct CPO. The misorientation axis distributions in crystal coordinates are very similar for all the different layers except for those containing the ribbon porphyroclasts, and show high density towards the c-axis orientation for both low and high (~60°) misorientations (2^{nd}-3^{rd} plots of Figs. 10b-f). For low angle misorientations the distribution of axes is broad with the maximum intensity increasing from the layers with peripheral directions (max = 1.6 multiple of uniform distribution, mud) to the intermediate directions (max = 2.29 mud) and to the Y-directions (max = 3.68 mud). For high angle misorientation the axes strongly concentrate around the c-axis orientation. In sample coordinates, the misorientation axes plots are also very similar for the different layers with misorientation axes clustered around Y, for low angle misorientations, and around the dominant c-axis orientation of the layer for high angle misorientations.

The mean (geometric) grain size of recrystallized grains in ultramylonites is ~ 9 μm with negligible differences between the layers with different CPO (Fig. SOM8). The recrystallized aggregates show a strong oblique SPO. Grains belonging to layers with a Y- and intermediate c-axis orientations have a slightly larger aspect ratio (Y-orientation: R mean = 3.06; σ = 1.26; intermediate-orientation: R mean = 2.92; σ = 1.29) than those with peripheral maximum (R mean = 2.38; σ = 1.05).

5.2.2 Ribbon porphyroclasts

Asymmetric ribbon porphyroclasts are common within recrystallized layers with peripheral c-axis maxima. (Figs. 10a, 10g and 10i) As described above, the asymmetry of the ribbon porphyroclast is opposite to that commonly shown by mineral fishes in mylonite (e.g. Pennacchioni et al., 2001; ten Grotenhuis et al., 2002). This shape derives from dissection of ribbon grains along μSZs that are sub-parallel to a rhombohedral planes and suitably oriented for being activated as C' shear bands. The internal distortion of the porphyroclasts is manifested by undulose extinction and zones of high subgrain density especially close to the porphyroclast tips.

The c-axes of the ribbon porphyroclasts plot along the periphery of the pole figure dispersed over a range of ~80° from directions nearly orthogonal to the ultramylonitic foliation to directions at a low angle to foliation in the NW-SE pole figure quadrant for this “dextral” quartz mylonite (Fig. 10g).

The recrystallized aggregate surrounding the ribbon porphyroclasts show a c-axis preferred orientation distributed along the pole figure periphery (Fig. 10h) with two c-axis maxima: (i) close to the c-axis orientation of the ribbon porphyroclast; and (ii) close to the peripheral maxima at the end of the CPO girdle visible in the bulk

The MAD for both the porphyroclast and the surrounding aggregate show a strong peaks at low (<15°) misorientations and a weaker one at about 60° (Figs. SOM7f-g). In crystal coordinates, the misorientation axes distributions of both porphyroclast and recrystallized aggregate show (2^{nd}-3^{rd} plots of Figs. 10g-h): (i) slightly higher density close to the periphery of the IPF along a {m} to <a> girdle and close to the c-axis for low angle misorientations; and (ii) high density around the c-axis for misorientations around 60°. In sample coordinates, the low angle misorientation axes cluster around Y, while the high angle misorientation axes overlap in orientation with the c-axis orientation (4^{th}-5^{th} plots of Figs. 10g-h).

6. CL imaging

The CL in quartz is a powerful tool for investigating microstructural complexity and possible signs of fluid-rock interaction (e.g. Bestmann and Pennacchioni, 2015). Two main observations come from CL investigation: (i) recrystallization in and polygonalization around μSZs are associated with a lower (darker) CL-signal that overprint the heterogeneous CL signal of protomylonitic quartz grains (Figs. SOM15a-f); (ii) ultramylonite textural domains are characterized by different CL signatures (Figs. SOM15g-h). Detailed results of CL investigations on Rieserferner quartz veins are reported in SOM.

7. Discussion

From ribbons to dynamic recrystallization

To a first approximation, the deformed quartz veins of Rieserferner show 2 main stages of evolution with increasing strain: (i) formation of ribbon grains at low strain, with only subordinate recrystallization; and (ii) ribbon dismantling by localized to pervasive dynamic recrystallization. Ribbons dominate the microstructure at low bulk strain ($\gamma < 2$) and recrystallization became widespread, for shear strain in a range between 3 and 6, to pervasive at $\gamma > 10$, when > 90% of the vein volume was converted to an aggregate of small (10 μm mean grain size) dynamically recrystallized grains. A similar evolution, from ribbon to fine-grained mylonites, was described for deformed quartz veins within tonalites of Adamello pluton (Pennacchioni et al., 2010) that formed and deformed in a similar context of pluton cooling as Rieserferner quartz veins. In Adamello, Pennacchioni et al. (2010) determined that transition from non-recrystallized elongate-ribbon grains to pervasively recrystallized veins occurred abruptly at $\gamma = 3$, a value roughly coinciding with the threshold for widespread recrystallization estimated for Rieserferner veins. This γ value is also remarkably similar to the effective shear strain recalculated in Heilbronner and Kilian (2017) for pervasive recrystallization of Black Hill Quartzite during the general shear experiments described by Heilbronner and Tullis (2006).

Non-recrystallized ribbon portions

The pristine quartz veins were coarse grained and, in protomylonites, each ribbon represents a stretched non-recrystallized crystal. Different initial crystallographic orientations of the vein crystals caused different deformation behaviours during vein boundary-parallel simple shear (e.g Bouchez, 1977; Mancktelow, 1981). Y-type ribbons behaved as the most plastically compliant grains and stretched to high aspect ratios without significant recrystallization (Figs. 2d-e). This implies that {m}<a> was the easy (most efficient in accommodating strain, and/or slip system with low critical resolved shear stress) slip system at the conditions of deformation, as also supported by the low angle misorientation axis distribution showing a relatively strong maximum close to c-axis in crystal coordinates (Fig. 6c) and the resulting maximum parallel to the Y-direction in sample coordinates. Boundary trace analysis (Prior et al., 2002; Piazolo et al., 2008) of subgrains with misorientation axes either around [c] and <m> are consistent with the local occurrence of both {m}<a> and (c)<a> slip (Fig. SOM7). Misorientation around <m> (oriented NE-SW in the pole figure of Fig. 6b) could also explain the dispersion into a girdle (orthogonal to <m>) of the c-axis by a distortional “tilting” or “flexural slip” along the basal plane with slip along the <a> nearly orthogonal to the misorientation axis (and roughly parallel to the shortening direction). This c-axis dispersion and the absence of a dispersion around the c-axis reflect the different efficiency of the 2 slip systems, with the favoured {m}<a> slip effectively accommodating crystal elongation and inducing negligible internal distortion of the ribbon.

The XZ- and Z-type ribbons derived from vein crystals with c-axis orthogonal to the Y-direction that should disadvantage the activity of {m}<a> slip. These ribbons were less strain-compliant than Y-types as indicated by their lower aspect ratio; the higher internal distortion resulted in faster hardening and in a higher degree of recrystallization at the same bulk strain. This is consistent with the experimental results of Muto et al. (2011) on synthetic single quartz crystals with different initial orientations chosen to activate the 3 main slip systems of quartz ((c)<a>, {m}<a>, and {m}[c] under the same experimental conditions) even though there are remarkable differences in the microstructural and CPO evolution in the experiments compared with our natural samples as it will be discussed below.

XZ- and Z-type ribbons experienced lattice distortion, formation of subgrains, and incipient recrystallization, and show a widespread occurrence of Dauphiné twinning. In XZ-types ribbons the internal distortion is manifested by a dispersion of crystallographic axes around the Y-direction (similarly to the dispersion of c-axis observed for non recrystallized domains in Muto et al.,2011). Part of the internal distortion was accomplished through rotations around low angle misorientation axes as indicated by the MAD (Figs. 9a-d). In all XZ-type ribbons, we infer that {m}<a> slip system still partially assisted intracrystalline deformation despite the unfavorable crystal orientation. This is suggested by the clustering of low angle misorientation axes towards the c-axis in crystal coordinates (Figs. 7e, 8e and SOM6c) and by trace analysis of a few subgrains (Fig. SOM10-12). As discussed for Y-type ribbons, the efficiency of {m}<a> slip resulted in a very minor lattice distortion associated with the misorientation around c-axis and this would explain the absence of any major dispersion of crystallographic axes around [c] in all pole figures of Figs. 7-SOM6. This interpretation is also supported by the fact that, in sub-plots of low angle misorientation axis distributions in crystal coordinates considering smaller ranges of misorientations (2-5°, 5-10° and 10-15°), the c-axis maxima are stronger at very low angle misorientations (Fig. SOM13-14).

In XZb-type ribbons, the distribution of low angle misorientation axis towards [c] in crystal coordinates is close to uniform (Fig. 8e).I In sample coordinates, this distribution results in an eccentric maximum with respect to Y that does not coincide with the c-axis position in the pole figure. This maximum rather coincides with the position of {r-z} suggesting that available slip systems (or combinations of slip systems) with misorientation axis close to the Y-direction were preferentially activated (e.g. Neumann, 2000; Lloyd et al., 2004; Morales et al., 2011). The heterogeneity in the deformation and activation of specific slip systems is illustrated by the analysis of the areas 1 and 2 of the same ribbon that show different types of distribution of low angle misorientation axes towards the c-axis and towards {r-z}. In the XZa-type ribbon of Fig. 7a the low angle misorientation axes distribution in sample coordinatesshows a distribution along a girdle between the two peripheral c-axis directions suggesting the activation of slip systems with misorientation axis close to the Y-direction.

In general terms, this preferential activation of slip system with misorientation axis close to the kinematic vorticity axis may be aided also by the elsatic and plastic anisotropic properties of quartz. The most compliant directions in quartz are close to <m> and <r>, whereas the most stiff directions are close to <z> (McSkimin et al., 1965; Menegon et al., 2011). This elastic anisotropy may be also reflected in the differential activation of slip system (Menegon et al., 2011), activating preferentially those slip system that exploit {m} or {r} planes.

Recrystallization within μSZs of XZ-type ribbons

In XZ-type ribbons, incipient recrystallization occurred along μSZs. These recrystallization microstructures have been already described for quartz and their origin has been interpreted in different ways (e.g. van Daalen et al., 1999; Vernooij et al., 2005, 2006a, b; Trepmann et al., 2007, 2017; Stipp and Kunze, 2008; Menegon et al., 2008, 2011; Derez et al., 2015; Kjøll et al., 2015). Similar μSZs have also been described in feldspars (Stünitz et al., 2003; Menegon et al., 2013) and in calcite (Bestmann and Prior, 2003; Rogowitz et al., 2016). The main characteristics of the μSZs in the quartz ribbons of the Rieserferner veins are summarized and discussed below.

a) The CPO of recrystallized aggregates of μSZs show a dispersion of the crystallographic axes, from the crystallographic orientations of the host grain, consistent with the sense of shear of the μSZs and with a rotational axis roughly coinciding with the vorticity axis of the shear zone (Y-axis). The amount of dispersion does not scale with μSZs thickness (and accommodated slip). In fact, large rotations of crystallographic ([c]) axes (~ 90°) are also observed for the new grains within incipient μSZs. As discussed above, a smaller, but similar dispersion of crystallographic axes is observed within the distorted host ribbon grains.
b) The MAD for evolved and mature μSZs include a wide range of misorientation angles between 10° and 60° (except the evolved μSZ ϕ: Fig. 9g).These MADs are significantly different from those of both the host ribbons and ultramylonites that show clear and strong peaks at low angle misorientations (< 15°) and around 60° (Figs. 9b-d and 9i).
c) The misorientation axis distributions for low angle misorientations include high density spots around different crystallographic orientations in the different μSZs (e.g. {m},{r-z},

and <a> for µSZ ε: Fig. 7g), but in sample coordinates higher density systematically occurs close, though slightly eccentric, to the Y-axis. Along with minor clustering towards the orientation of the c-axis they tend to form a girdle. ; showing also some correlation with misorientation axis distributions ofof the host ribbon. The eccentricity of the maximum is interpreted to reflect either the deviation of the local vorticity vector with respect to the bulk vorticity vector of the sample (i.e., the Y-axis), or the difficulty to precisely place the sample coordinate frame in a protomylonite and exactly cut the sample parallel to the principal kinematic sections (or both factors). High density of the low angle misorientation axes “close to Y” therefore implies a main rotation parallel to the vorticity axis with some preferential activation of well-oriented slip systems. This rotation of subgrains, controlled by the vorticity axis, is supported by the fact that also high angle misorientations (15-45°) between new grains within the µSZs show very similar maxima close to Y (Fig. SOM6). This suggests the occurrence of a purely kinematic “rigid body” rotation of the new grains around Y (e.g. Bestmann and Prior, 2003; Trepmann et al., 2007; Stipp and Kunze, 2008). A feature less easy to interpret is the dispersion of the misorientation axes to form a girdle in sample coordinates nearly orthogonal to grain SPO especially in mature µSZs (e.g. µSZs ε, Fig. 7g, and ξ, Figs. SOM6e-h). In the µSZ ε (Fig. 7) the girdle is clearly subparallel to the trace of the subgrain and grain boundaries internal to the elongated grains .

d) Dauphiné twinning occurred pervasively within the host ribbons, but the orientation of µSZs is not systematically linked to Dauphiné twin boundaries in contrast to what was reported by Menegon et al. (2011).

e) There is crystallographic control on the orientation of the µSZs whose trend is subparallel to the trace of {r-z}, {m} or (c), as reported in van Daalen et al. (1999), Vernooij et al. (2006a, b) and Kjøll et al. (2015). Negative rhombs <z> are the least compliant crystallographic directions in quartz (in terms of its anisotropic elastic properties, McSkimin et al., 1965; Menegon et al., 2011) and they may act as site of accumulation of dislocation and defects promoting recovery processes and/or micro-fracturing along them.

f) The grain size of the new grains is in the range between 10 and 20 µm for the differently evolved μSZs and is similar to the mean (geometric) grain size of the ultramylonitic recrystallized matrix (10 μm). In the μSZs the grain size of new grains is similar to the size of the subgrains locally developed at the boundary of the μSZs (e.g. Bestmann and Prior, 2003; Trepmann et al., 2007). This supports the occurrence of a component of SGR recrystallization during incipient μSZ nucleation or at the moving μSZs boundary during progressive strain accumulation (e.g. Halfpenny et al., 2012). The size of the new recrystallized grains in the μSZs was determined by the occurrence of recovery processes in the parent grains and cannot therefore be completely ascribed to a cataclastic process which has been inferred to occur during initial stages of μSZ development by some authors (e.g. van Daalen et al., 1999; Vollbrecht et al., 1999; Kjøll et al., 2015)

g) The μSZs were preferentially infiltrated by fluids and formed the backbones for fluid redistribution into the host ribbons as indicated by (i) the clustering of fluid inclusions along the μSZs; and (ii) the pervasive resetting of the CL signature along and nearby μSZs (e.g. Fig. SOM15e). The presence of mica, precipitated along incipient μSZs and deformed within the aggregate of more evolved μSZs (Figs. SOM3c-d), suggests that part of the fluid infiltration did not just post-date shearing. There are not evident fluid-inclusion trails within the host ribbon subparallel to the μSZs that could support the hypothesis of an origin of the μSZs from nucleation on precursor, healed microcracks.

Strain hardening of XZ-type ribbons resulted in development of crystallographically-controlled μSZs. We infer that initial recrystallization along the μSZs is associated with SGR as indicated by: (i) the discontinuous presence of a zone of subgrain polygonization in the host ribbon flanking the μSZs (e.g. Bestmann and Prior, 2003); and (ii) by the similarity in size between the host ribbon subgrains and recrystallized new grains. The MADs of μSZs show a wide range of high misorientation angles that indicate the occurrence of a concurrent deformation mechanism together with the incipient SGR. This concurrent mechanism must be at the base of the sudden change in orientation of new grains within μSZs to the host and neighbour grains since the incipient stages of recrystallization and is indicated by a rotation of crystallographic axes preferentially around the vorticity axis Y, but also around other directions (third column of Fig. SOM6). This mechanism apparently became inactive in mylonites/ultramylonites despite the similarity in grain size of recrystallized aggregates. We envisage that process of grains reorientation within the μSZs as a "rigid-body" rotation of grains, initiated as subgrains by SGR, related to the geometric roughness of the μSZs and to the confined slip along the μSZs (similarly to the model presented by Trepmann et al., 2017). This process is essentially an example of viscous grain boundary sliding which is in part kinematically-controlled by the orientation of the local vorticity axis. The roughness results from both the heterogeneous degree of subgrain/new grain evolution along the μSZs that is renewed by continuous formation of new subgrains at the μSZs. Thickening of the μSZs in fact occurred by progressive incorporation of the host ribbon selvages and in mature shear zones the aggregate at the core of the shear zone experienced higher degree of rotation, as shown by van Daalen et al. (1999) in similar μSZs in quartz (e.g. Fig. SOM6). Probably, thickening of the recrystallized aggregate decreased the influence of the geometric roughness during confined shear and the efficiency of "rigid body" rotation mechanisms, leeaving the complete control on recrystallization process to SGR recrystallization in mature μSZs and in the following stages of mylonitization.

Our observation and interpretation are very similar to the results of Kjøll et al., (2015), who describe the development of localized recrystallization along crystallographycally-controlled features similar to μSZs in hardened quartz grains. Despite the similarities, we do not observe striking evidence for cyclical embrittlement induced by fluid pressure oscillation or the evidence for pressure-solution processes as suggested by Kjøll et al. Lack of (unexploited) fluid inclusion trails point to a different origin for μSZs. Initial brittle processes and micro-cataclasis locally induced by anisotropic rheological properties of quartz may explain some of the above described characteristics (e.g. high angle misorientation of new grains in incipient μSZs) but we do not observe any other evidence for it.

The observations from the Rieserferner deformed quartz veins are difficult to reconcile with many experimental results of Muto et al. (2011). We observe, as in their experiments, that the initial crystallographic orientation of the crystals resulted in a different strength of the grains that promoted recrystallization of XZ-type ribbons badly oriented for easy glide. However, Muto et al. (2011) observed the development of distinct domains of recrystallized grains with a Y-max CPO in all crystals independently of the starting crystallographic orientation, which is not found in the Rieserferner veins. In the experiments recrystallization within crystals with {m}[c] and (c)<a> orientations was not spatially organized into μSZs as in the Rieserferner XZ-type ribbons.

Ultramylonitic quartz veins

The quartz ultramylonites consist of a fine-grained aggregate of recrystallized grains. A typical feature of mylonite and ultramylonite is the presence of CPO banding that is interpreted to be inherited from the former vein quartz crystals and to derive from recrystallization of ribbons (and therefore of vein crystals) with different original crystallographic orientations (e.g. Pauli et al., 1996; Lloyd et al., 1992; Pennacchioni et al., 2010; Morales et al., 2011; Price et al., 2016) persisting up to very high strains ($\gamma > 10$). The bulk c-axis CPO of the pervasively recrystallized ultramylonites is comparable in type to the CPO of the ribbon protomylonites and shows a girdle at a high angle to the mylonitic foliation (slightly inclined to the foliation normal according with sense of shear) and a wide peripheral spreading becoming more rarefied close to the foliation. The mean (geometric) grain size of recrystallized grains (~ 10 μm), almost identical within the different layers (at the contrary of Heilbronner and Tullis, 2006), is comparable (albeit slightly smaller and more homogeneous) with the recrystallization grain size within the μSZs of XZ-type ribbons. This suggests that, throughout the whole deformation/recrystallization history and in all microstructures, the recrystallized grain size was controlled by subgrain formation and recrystallization by SGR (as also indicated by MAD; e.g. Halfpenny et al., 2012). Despite there was a clear difference in strength between the differently oriented ribbons in the protomylonites, there is not a consequent variation in subgrain and new grain sizes that should be expected according to grain size piezometry (Stipp and Tullis, 2003). The individual misorientation axes distribution in crystal coordinates for the layers with different CPO all show a more or less broad clustering towards the c-axis, that is however weaker for the layers with a dominance of peripheral orientations (e.g. layers I and II of Fig. 10). The misorientation axis distributions in sample coordinates shows, for all layers, that the slip systems with misorientation axes well aligned with the Y-axis of the shear zones were preferentially activated and indicate a control of the bulk shear zone kinematic framework on recrystallization.

In Rieserferner ultramylonites, despite the evidence that the favoured slip system was {m}<a>, there is no indication of any relevant strain partitioning between layers with different CPO in recrystallized aggregates and therefore of significant strength differences of recrystallized aggregates (as instead proposed by Heilbronner and Tullis, 2006; Toy et al., 2008; Muto et al., 2011). In Rieserferner ultramylonites there is no evidence of cannibalism of {m}<a> against the other slip systems, at least for the range of investigated strain and no significant reset of the CPO occurred. As recalled above, the microstructure appears homogeneous in terms of grain size and show only minor differences in the grain aspect ratios. These observations are not dissimilar from the conclusions of Pennacchioni et al. (2010), who also noted that (i) dynamic recrystallization, occurring rather abruptly in a range of γ between 2 and 3, did not significantly altered the CPO from weakly deformed ribbon mylonites to strongly deformed and pervasively recrystallized veins; and (ii) initial crystal orientations badly oriented for dominant {m}<a> persisted up to high strain.

In the experiments of Muto et al. (2011) on synthetic single crystals all the different starting orientations developed distinct domains of recrystallized grains with c-axis Y-maximum CPO and the area of these domains increased with increasing bulk shear strain and extent of dynamic recrystallization. They noted that there was a reset from the initial {m}[c] and (c)<a> orientations that was basically complete for 100% recrystallization and $\gamma < 3$. In practice, these experiments imply that a quartz vein with initial random orientation of crystals would end up at relatively low strain in a homogeneous quartz ultramylonite with strong Y-max CPO without any inheritance from the original microstructure. This is in stark contrast with the evolution derived for the Rieserferner sheared quartz veins and other natural examples (e.g. Pennacchioni et al., 2010; Rahl and Skemer, 2016). A main reason for such contrast could be the difference in recrystallization mechanism and/or fluid conditions in the experimental/natural case. As pointed out by Muto et al. (2011) replacement of the original crystal orientation by growth of more favourable (Y-maximum) orientations requires grain boundary migration, whereas the Rieserferner veins were deformed in a dominant SGR regime. At natural strain rates, the experimental conditions of Muto et al. (2011) likely extrapolate to temperatures slightly higher than those estimated for deformation in the Rieserferner quartz veins (i.e. ca. 450 °C). The dominance of SGR during shearing may also explain, in part, the presence of a CL banding in ultramylonites that we interpret as difference in Ti concentration between the different layers. As described by Bestmann and Pennacchioni (2015) dominant SGR is not efficient in completely resetting the Ti concentrations even at stages of pervasive deformation. The CL signature associated with the deformation microstructures of the Rieserferner veins are however suggestive of more water-rich conditions compared with the Sierra Nevada sample of Bestmann and Pennacchioni (2015).

8. Conclusions

Mylonitization of coarse grained quartz veins resulted in a complex evolution during deformation at temperature of ~ 450 °C, in large part derived by the initially different crystallographic orientations of the vein crystals. The following points summarize the main results of the study.

- Depending on the initial crystallographic orientations vein crystals manifested, in early stages of shearing, different strengths resulting in distinct aspect ratios and degree of incipient recrystallization of developing ribbon grains. The most favourably oriented crystals were Y-type ones, indicative that {m}<a> was the easy slip system. Ribbons with c-axis orthogonal to Y underwent early hardening and recrystallized along conjugate sets of crystallographically-controlled μSZs.
- Recrystallization in μSZs initiated most likely by SGR. Once formed, new grains rotated around Y (up to misorientations > 90°), accordingly with the μSZ shear sense, since the incipient μSZ slip. Distorted ribbons show a similar (but lower) rotational spreading of

crystallographic axes. This rotational CPOs resulted from both the preferential activity of slip systems which formed subgrain boundaries with a misorientation axis coinciding with Y (especially in the host ribbon) and passive grain rotation.

- Grain rotation within the μSZs was associated with the confined shear.
- Pervasive recrystallization and high shear strains were not capable of resetting the initial texture to a c-axis Y-maximum CPO as it would be expected from the evidence of the preferential activity of {m}<a> slip. Quartz ultramylonites show a domainal texture inherited from deformation and recrystallization of original crystals with a different CPO.
- In ultramylonites the misorientation angle/axis plots indicate that recrystallization by dominant SGR was assisted by the preferential activity of slip systems which formed subgrain boundaries with a misorientation axis parallel to Y, though {m}<a> was still the most efficient slip system, and/or passive rotation around Y.
- Within the different domains, grains with c-axis parallel to Y did not grow "rapidly" with increasing strain at the expenses of other grains in contrast to what is observed in the experiments of Muto et al. (2011). If a selective replacement by Y-grains of other grains did effectively occur with strain accumulation, the process was sluggish.
- The grain size of recrystallized grains does not depend significantly on (i) the amount of strain and degree of recrystallization; (ii) the CPO of the parent ribbon grain (protomylonite) or of the recrystallized layers (ultramylonite). This contrasts with the observation the inferred strength between ribbons and with the evidence of preferential {m}<a> slip.

Acknowledgements

Rudiger Kilian and Reneé Heilbronner are thanked for the assistance and guidance with the CIP analysis. Giulia Degli Alessandrini, Anna Rogowitz are thanked for discussion. Financial support from the University of Padova ("Progetto di Ateneo" CPDA140255) and from the Foundation "Ing. Aldo Gini" is acknowledged.

Appendix – Methods and Analytical techniques

CIP Microscopy / Image Analysis / Microstructural feature quantification

Computer-integrated polarization microscopy (CIP: Heilbronner and Pauli, 1993) was mainly aimed at evaluating the c-axis orientation of the coarse grained ribbon protomylonites. The CIP microphotographs were acquired on a Zeiss Axioplan, with attached a Basler Ace (acA1600-20gm) camera, at the Institute of Geology and Paleontology of Basel University (Switzerland). Areas of 20 mm^2 were imaged with a resolution of ~ 3µm/pixel with a magnification of 2.5x each. To obtain a bulk pole figure of representative areas of the thin section, microphotographs were stitched (with a consequent decrease in resolution) and then processed with the CIP software suite for texture analysis and orientation imaging. Crystallographic orientations are plotted on equal area, lower hemisphere pole figures.

Optical images and processed EBSD maps were analysed in some cases with Paror and Surfor (FABRIC software suite, Heilbronner and Barret, 2014) to estimate grain shapes, shape preferred orientations and the orientation of µSZs (reported in rose diagram in Fig.4 and SOM1C)

Several scan images of the same thin section (no polarizer, crossed polarized, gypsum-plate inserted and CIP images) have been compared and analysed by image analysis to define the areal extension of each ribbon, its bulk c-axis orientation and its microstructural features (Aspect Ratio; AR; Recrystallization amount: Rexx%, given as area fraction, Area%). These methods have some limitation: (1) image optical resolution and the possibility to discern localized recrystallization features. For example, Rexx% quantification (Fig. 2e) in those cases where the recrystallization is localized it represent a good approximation of the real value, whereas where the recrystallization is scattered and irregularly distributed all over the ribbon, this values represent a minimum estimation. (2) Thin section dimensions commonly are too small to contain mm-cm ribbons. The reported AR value (Fig. 2d) is therefore a minimum value of AR.

EBSD analysis

Electron backscattered diffraction analysis was carried out with: (i) FEG-SEM Zeiss 1540 EsB (Flamenco acquisition software, Oxford Instruments) at the Material Science Department – Geozentrum Nordbayern Erlangen; and (ii) JEOL 6610 LV SEM equipped with a NordLys Nano EBSD detector (AZTec acquisition software, Oxford Instruments); and (iii) JEOL 7001 FE SEM equipped with a NordLys Max EBSD detector (AZTec acquisition software, Oxford Instruments) at the Electron Microscope Centre of Plymouth University. Each thin section was SYTON-polished for at least 6 hours and carbon coated (about 3.5nm coating thickness). Analytical conditions, steps size, acquisition rates and other map characteristics are reported for each individual map in Table SOM1. All data have been processed (noise reduction following e.g. Bestmann and Prior, 2003) and analysed using CHANNEL5 software of HKL Technology, Oxford Instruments.

Monoclinic sample symmetry has been used. Quartz was the only mineral phase to be indexed, using trigonal symmetry (Laue group -3m). Critical misorientation for the distinction between low- and high-angle boundaries have been chosen at 15°, allowing grain boundary completion down to 0°. In addition, grain boundaries with 60°±5° of misorientation were disregarded from grain detection procedure, to avoid any contribution from Dauphiné twinning in the definition of grains.

The pole figures and the misorientation axis distributions in sample coordinates are equal area, lower hemisphere projections oriented with the general shear zone kinematics reference system (X = stretching lineation; Z = pole to general shear plane/vein boundary). The inverse pole figures for misorientation axis distribution in crystal coordinates are upper hemisphere projections.

Grain size analysis

Grain sizes are obtained from the grain detection routine in Channel5 Tango software. Equivalent grain diameters are obtained from grain area (μm^2). The minimum cut-off area below which grains are not considered have been set to 1 μm^2; therefore only grains composed of 4 to 9 pixels (according to map acquisition step-size) have been considered. Grain size data are then plotted as area-weighted distributions as frequency against square-root grain-size-equivalent grain diameters (as in Herweg and Berger 2004). The grain size distribution is close to a Gaussian distribution when plotte din this way, therefore it gives us a good estimation of the mean grain size. The geometric mean grain size is obtained graphically as the maximum frequency grain size of the distribution curve. The distribution curve is obtained interpolating distribution data with a 6^{th} degree polynomial equation in Excel-MS Office. The arithmetic mean, instead, have been calculated directly from the equivalent grain diameter database without any area-weighting process.

Subgrain size have been determined in the same way but, setting the critical misorientation at 2° in Channel5 Tango grain detection routine. Then, only those subgrains useful for the analyses (those close to the μSZs) have been manually selected.

References

Bellieni, G., 1978. Caratteri geochimici del massiccio granodioritico tonalitico delle Vedrette di Ries (Rieserferner) - Alto Adige Orientale. Rendiconti della Società Italiana di Mineralogia e Petrologia 34, 527-548.

Berger, A., Herwegh, M., Schwarz, J. O., and Putlitz, B., 2011. Quantitative analysis of crystal/grain sizes and their distributions in 2D and 3D. Journal of Structural Geology 33, 1751-1763.

Bestmann, M., Prior, D.J., 2003. Intragranular dynamic recrystallization in naturally deformed calcite marble: diffusion accommodated grain boundary sliding as a result of subgrain rotation recrystallization. Journal of Structural Geology 25, 1597-1613.

Bestmann, M., Pennacchioni, G., 2015. Ti distribution in quartz across a heterogeneous shear zone within a granodiorite: The effect of deformation mechanism and strain on Ti resetting. Lithos 227, 37-56, doi:10.1016/j.lithos.2015.03.009.

Bouchez, J.-L., 1977. Plastic deformation of quartzites at low temperature in an area of natural strain gradient. Tectonophysics 39, 25-50, doi:10.1016/0040-1951(77)90086-5.

Cesare, B., 1994. Hercynite as the product of staurolite decomposition in the contact aureole of Vedrette di Ries, eastern Alps, Italy. Contributions to Mineralogy and Petrology 116, 239-246.

Dell'Angelo, L.N., Tullis, J., 1989. Fabric development in experimentally sheared quartzites. Tectonophysics 169, 1-21.

Derez, T., Pennock, G., Drury, M., Sintubin, M., 2015. Low-temperature intracrystalline deformation microstructures in quartz. Journal of Structural Geology 71, 3-23.

Gleason, G.C., Tullis, J., 1995. A flow law for dislocation creep of quartz aggregates determined with the molten-salt cell. Tectonophysics 247, 1-23.

Gleason, G. C., Tullis, J., Heidelbach, F., 1993. The role of dynamic recrystallization in the development of lattice preferred orientations in experimentally deformed quartz aggregates. Journal of Structural Geology 15, 1145-1168.

Halfpenny, A., Prior, D. J., Wheeler, J., 2012. Electron backscatter diffraction analysis to determine the mechanisms that operated during dynamic recrystallisation of quartz-rich rocks. Journal of Structural Geology 36, 2-15.

Heilbronner, R. P., Pauli, C., 1993. Integrated spatial and orientation analysis of quartz c-axes by computer-aided microscopy. Journal of Structural Geology 15, 369-382.

Heilbronner, R., Tullis, J., 2006. Evolution of c axis pole figures and grain size during dynamic recrystallization: Results from experimentally sheared quartzite, Journal of Geophysical Research 111, B10202, doi:10.1029/ 2005JB004194.

Heilbronner, R., & Barrett, S. (2014).Image analysis in earth sciences: microstructures and textures of earth materials . Springer Science & Business Media.

Heilbronner, R., Kilian, R., 2017. The grain size(s) of Black Hills Quartzite deformed in the dislocation creep regime. Solid Earth Discussion, doi:10.5194/se-2017-30

Herwegh, M., & Berger, A., 2004. Deformation mechanisms in second-phase affected microstructures and their energy balance. Journal of structural geology 26, 1483-1498.

Hirth, G., Teyssier, C., Dunlap, W.J., 2001. An evaluation of quartzite flow laws based on comparisons between experimentally and naturally deformed rocks. International Journal of Earth Sciences 90, 77-87, doi:10.1007/s005310000152

Hirth, G., Tullis, J., 1992. Dislocation creep regimes in quartz aggregates. Journal of Structural Geology 14, 145-159.

Hobbs, B.E., 1968. Recrystallization of single crystals of quartz. Tectonophysics 6, 353-401.

Kilian, R., Heilbronner, R., Stünitz, H., 2011. Quartz grain size reduction in a granitoid rock and the transition from dislocation to diffusion creep. Journal of Structural Geology 33, 1265-1284, doi:10.1016/j.jsg.2011.05.004

Kjøll, H.J., Viola, G., Menegon, L., Sørensen, B.E., 2015. Brittle–viscous deformation of vein quartz under fluid-rich low greenschist facies conditions. Solid Earth 7, 213-257.

Lloyd, G. E., Law, R. D., Mainprice, D., Wheeler, J., 1992. Microstructural and crystal fabric evolution during shear zone formation. Journal of Structural Geology 14, 1079-1100.

Lloyd, G. E., 2004. Microstructural evolution in a mylonitic quartz simple shear zone: the significant roles of dauphine twinning and misorientation. Geological Society of London, Special Publications 224, 39-61.

Luan, F.C., Paterson, M.S. ,1992. Preparation and deformation of synthetic aggregates of quartz. Journal of Geophysical Research 97, 301-320.

Mancktelow, N.S., 1981. Strain variation between quartz grains of different crystallographic orientation in a naturally deformed metasiltstone. Tectonophysics 78, 73-84.

Mancktelow, N.S., Stöckli, D.F., Grollimund, B., Müller, W., Fügenschuh, B., Viola, G., Villa, I. M., 2001. The DAV and Periadriatic fault systems in the Eastern Alps south of the Tauern window. International Journal of Earth Sciences 90, 593-622.

Mancktelow, N.S., Pennacchioni, G., 2004. The influence of grain boundary fluids on the microstructure of quartz-feldspar mylonites. Journal of Structural Geology 26, 47-69.

Mancktelow, N.S., Pennacchioni, G., 2005. The control of precursor brittle fracture and fluid–rock interaction on the development of single and paired ductile shear zones. Journal of Structural Geology 27, 645-661.

Mancktelow, N.S., Pennacchioni, G., 2010. Why calcite can be stronger than quartz. Journal of Geophysical Research 115, B01402, doi:10.1029/2009JB006526.

Menegon, L., Pennacchioni, G., Heilbronner, R., Pittarello, L., 2008. Evolution of quartz microstructure and c-axis crystallographic preferred orientation within ductilely deformed granitoids (Arolla unit, Western Alps). Journal of Structural Geology 30, 1332-1347.

Menegon, L., Pennacchioni, G., 2010. Local shear zone pattern and bulk deformation in the Gran Paradiso metagranite (NW Italian Alps). International Journal of Earth Sciences 99, 1805-1825, doi:10.1007/s00531-009-0485-6

Menegon, L., Piazolo, S., Pennacchioni, G., 2011. The effect of Dauphiné twinning on plastic strain in quartz. Contributions to Mineralogy and Petrology 161, 635-652.

Menegon, L., Stünitz, H., Nasipuri, P., Heilbronner, R., Svahnberg, H., 2013. Transition from fracturing to viscous flow in granulite facies perthitic feldspar (Lofoten, Norway). Journal of Structural Geology 48, 95-112.

Morales, L. F., Mainprice, D., Lloyd, G. E., Law, R. D., 2011. Crystal fabric development and slip systems in a quartz mylonite: an approach via transmission electron microscopy and viscoplastic self-consistent modelling. Geological Society of London, Special Publications 360, 151-174.

Muto, J., Hirth, G., Heilbronner, R., Tullis, J., 2011. Plastic anisotropy and fabric evolution in sheared and recrystallized quartz single crystals. Journal of Geophysical Research 116, B02206, doi:10.1029/2010JB007891

Neumann, B., 2000. Texture development of recrystallised quartz polycrystals unravelled by orientation and misorientation characteristics. Journal of Structural Geology 22, 1695-1711.

Pauli, C., Schmid, S. M., Heilbronner, R. P., 1996. Fabric domains in quartz mylonites: localized three dimensional analysis of microstructure and texture. Journal of Structural Geology 18, 1183-1203.

Pennacchioni, G., Di Toro, G., Mancktelow, N.S., 2001. Strain-insensitive preferred orientation of porphyroclasts in Mont Mary mylonites. Journal of Structural Geology 23, 1281-1298, doi: 10.1016/S0191-8141(00)00189-9

Pennacchioni, G., 2005. Control of the geometry of precursor brittle structures on the type of ductile shear zone in the Adamello tonalites, Southern Alps (Italy). Journal of Structural Geology 27, 627-644.

Pennacchioni, G., Mancktelow, N.S., 2007. Nucleation and initial growth of a shear zone network within compositionally and structurally heterogeneous granitoids under amphibolite facies conditions. Journal of Structural Geology 29, 1757-1780.

Pennacchioni, G., Menegon, L., Leiss, B., Nestola, F., Bromiley, G., 2010. Development of crystallographic preferred orientation and microstructure during plastic deformation of natural coarse-grained quartz veins. Journal of Geophysical Research, Solid Earth 115, B12405, doi: 10.1029/2010JB007674.

Pennacchioni, G., Zucchi, E., 2013. High temperature fracturing and ductile deformation during cooling of a pluton: The Lake Edison granodiorite (Sierra Nevada batholith, California). Journal of Structural Geology 50, 54-81.

Piazolo, S., Montagnat, M., Blackford, J.R., 2008. Sub-structure characterization of experimentally and naturally deformed ice using cryo-EBSD. Journal of Microscopy 230, 509-519.

Price, N. A., Song, W. J., Johnson, S. E., Gerbi, C. C., Beane, R. J., West, D. P., 2016. Recrystallization fabrics of sheared quartz veins with a strong pre-existing crystallographic preferred orientation from a seismogenic shear zone. Tectonophysics 682, 214-236.

Prior, D. J., Wheeler, J., Peruzzo, L., Spiess, R., Storey, C., 2002. Some garnet microstructures: an illustration of the potential of orientation maps and misorientation analysis in microstructural studies. Journal of Structural Geology 24, 999-1011.

Rahl, J. M., Skemer, P., 2016. Microstructural evolution and rheology of quartz in a mid-crustal shear zone. Tectonophysics 680, 129-139.

Ramsay, J.G., 1980. Shear zone geometry: a review. Journal of Structural Geology 2, 83-99.

Ranalli, G., 2000. Rheology of the crust and its role in tectonic reactivation. Journal of

Geodynamics 30, 3–15.

Rogowitz, A., White, J. C., Grasemann, B., 2016. Strain localization in ultramylonitic marbles by simultaneous activation of dislocation motion and grain boundary sliding (Syros, Greece). Solid Earth 7, 355-366, doi:10.5194/se-7-355-2016

Romer, R.L., Siegesmund, S., 2003. Why allanite may swindle about its true age. Contributions to Mineralogy and Petrology 146, 297-307.

Rosenberg, C., 2004. Shear zones and magma ascent: a model based on a review of the Tertiary magmatism in the Alps. Tectonics 23, TC3002, doi:10.1029/2003TC001526

Schmid, S.M., Casey, M., 1986. Complete fabric analysis of some commonly observed quartz c-axis patterns. In: Mineral and Rock Deformation: Laboratory Studies – The Paterson Volume (eds B. E. Hobbs & H. C. Heard), pp. 263–86. American Geophysical Union, Geophysical Monograph vol. 36. Washington, DC, USA.

Steenken, A., Siegesmund, S., Heinrichs, T., 2000. The emplacement of the Rieserferner Pluton (Eastern Alps, Tyrol): constraints from field observations, magnetic fabrics and microstructures. Journal of Structural Geology 22, 1855-1873.

Stipp, M., Kunze, K., 2008. Dynamic recrystallization near the brittle-plastic transition in naturally and experimentally deformed quartz aggregates. Tectonophysics 448, 77-97.

Stipp, M., Tullis, J., 2003. The recrystallized grain size piezometer for quartz. Geophysical Research Letters 30, 2088, doi:10.1029/2003GL018444, 2003

Stipp, M., Stünitz, H., Heilbronner, R., Schmid, S.M., 2002. The Eastern Tonale fault zone: A “natural laboratory” for crystal plastic deformation of quartz over a temperature range from 250 °C to 700 °C. Journal of Structural Geology 24, 1861-1884, doi:10.1016/S0191-8141(02)00035-4.

Stünitz, H., Gerald, J. F., Tullis, J., 2003. Dislocation generation, slip systems, and dynamic recrystallization in experimentally deformed plagioclase single crystals. Tectonophysics, 372, 215-

233.

ten Grotenhuis, S.M., Passchier, C.W., Bons, P.D., 2002. The influence of strain localisation on the rotation behaviour of rigid objects in experimental shear zones. Journal of Structural Geology 24, 485-499.

Toy, V.G., Prior, D.J., Norris, R.J., 2008. Quartz fabrics in the Alpine Fault mylonites: Influence of pre-existing preferred orientations on fabric development during progressive uplift. Journal of Structural Geology 30, 602-621, doi:10.1016/j.jsg.2008.01.001.

Trepmann, C.A., Stöckhert, B., Dorner, D., Moghadam, R. H., Küster, M., Röller, K., 2007. Simulating coseismic deformation of quartz in the middle crust and fabric evolution during postseismic stress relaxation – an experimental study. Tectonophysics, 442, 83-104.

Trepmann, C.A., Hsu, C., Hentschel, F., Döhler, K., Schneider, C., Wichmann, V., 2017. Recrystallization of quartz after low-temperature plasticity – The record of stress relaxation below the seismogenic zone. Journal of Structural Geology, 95, 77-92.

Tullis, J., 1977. Preferred orientation of quartz produced by slip during plane strain. Tectonophysics 39, 87-102.

Tullis, J., Christie, J., Griggs, D., 1973. Microstructures and preferred orientations of experimentally deformed quartzites. Geological Society of America Bulletin 84, 297-314.

van Daalen, M., Heilbronner, R., Kunze, K., 1999. Orientation analysis of localized shear deformation in quartz fibres at the brittle–ductile transition. Tectonophysics 303, 83-107.

Vernooij, M.G., 2005. Dynamic recrystallisation and microfabric development in single crystals of quartz during experimental deformation (Doctoral dissertation, Diss., Naturwissenschaften, Eidgenössische Technische Hochschule ETH Zürich, Nr. 16050, 2005).

Vernooij, M.G., Kunze, K., den Brok, B., 2006a. 'Brittle' shear zones in experimentally deformed quartz single crystals. Journal of Structural Geology 28, 1292-1306.

Vernooij, M.G., den Brok, B., Kunze, K., 2006b. Development of crystallographic preferred orientations by nucleation and growth of new grains in experimentally deformed quartz single crystals. Tectonophysics 427, 35-53.

Vollbrecht, A., Stipp, M., Olesen, N. Ø., 1999. Crystallographic orientation of microcracks in quartz and inferred deformation processes: a study on gneisses from the German Continental Deep Drilling Project (KTB). Tectonophysics 303, 279-297.

Wagner, R., Rosenberg, C.L., Handy, M.R., Möbus, C., Albertz, M., 2006. Fracture-driven intrusion and upwelling of a mid-crustal pluton fed from a transpressive shear zone - The Rieserferner Pluton (Eastern Alps). Geological Society of America Bulletin 118, 219-237.

Figure captions

Fig. 1 - Polished slabs of sheared quartz veins of the Rieserferner pluton. The vein boundary is horizontal and the sense of shear is dextral (as can be inferred from the internal oblique foliation) for all samples. (a) Protomylonite showing a coarse, irregularly developed foliation defined by elongated to ribbon grains. The mean foliation inclination indicates a bulk shear strain $\gamma \simeq 1$. (b) Mylonitic vein with a more homogeneous oblique foliation corresponding to a bulk shear strain $\gamma \simeq 3.4$. (c) Ultramylonitic vein within a weakly deformed host tonalite localizing shear strain $\gamma > 10$.

Fig. 2 - Microstructure and CPO of protomylonitic quartz vein. (a) Optical microphotograph (crossed polarizers and inserted gypsum plate) of a thin section from the protomylonite shown in Fig. 1a. (b) Sketch drawn from (a) showing the different ribbons (in different colours) and incipient recrystallization aggregates (in black colour). The ribbons are colour-coded as a function of the dominant c-axis orientation determined by CIP analysis, accordingly with the Look-Up Table (LUT) reported in (c). (c) Pole figure (with a coloured LUT background) of the c-axis orientations (small black circles) of the ribbons in the 2 analysed thin sections of protomylonite (see also Fig. SOM1). The dashed line represents the trace of the average ribbon elongation. (d) Aspect ratios for the different ribbon orientations. The aspect ratio values larger and lower than the mean value (6~7) are evidenced in black and red characters, respectively. Underlined bold values represent actual aspect ratios for ribbons completely included within the thin section. (e) Area fractions of recrystallized aggregates for to the different c-axis orientations of the host ribbons. The red and black values represent values larger and smaller than the bulk sample recrystallization (~10%), respectively. High values occur mostly along the periphery of the pole figure. Low values dominate close to the centre of the pole figure.

Fig. 3 – Optical microstructures of ribbons in the protomylonite with a schematic representation of the [c] axis orientation determined by CIP analysis (lower-left pole figures). (a) Cross-polarized microphotograph of a dark-gray to black Y-type ribbon almost free of recrystallization. (b) Cross-polarized microphotograph of a Z-type ribbon with sharp longitudinal discontinuities sub-parallel to

the ribbon elongation and incipient recrystallization. Recrystallization occurred along the sharp discontinuities (some are indicated by white arrows) and, in the most strained part of the ribbon (down right), along conjugate microshear zones dominate by a synthetic Riedel-type set. (c) Microphotograph (crossed polarizers and inserted gypsum plate) of a XZa-type ribbon showing two sets of µSZs. (d) Cross-polarized microphotograph of XZb-type ribbon with two sets of µSZs. (e) CIP-derived c-axis orientation map of the microstructure in (c) coloured according the LUT (equal area, lower hemisphere). (f) CIP-derived c-axis orientation map of the microstructure in (d) coloured according the LUT. (g) c-axis CPO of the domain in (e) determined by CIP. (h) c-axis CPO of the domain in (f) determined by CIP.

Fig. 4 –Analysis of the orientations of fine-grained recrystallized aggregates in some ribbons of the protomylonite of Fig. 2b. A similar analysis of the 2nd studied protomylonite sample is reported in Fig. SOM1c. The orientations of the µSZs in the selected areas (surrounded by the dashed line and showing un-blurred colour) are shown in the rose diagrams.

Fig. 5 – Optical microstructures and c-axis orientation map (from CIP) of a quartz mylonite and ultramylonite. (a) Circular polarization microphotograph of mylonite showing the alternation of un-recrystallized to partly recrystallized ribbons and lens-shaped domains, and completely recrystallized matrix. (b) c-axis orientation map (from CIP analysis) of the image in (a) showing the LUT in the lower left corner. (c) CIP-determined c-axis pole figures for non recrystallized ribbons of (b). (d) CIP-determined c-axis pole figure for recrystallized matrix of (b). (e) Cross-polarized microphotograph of a pervasively recrystallized quartz ultramylonite showing an extinction banding of the matrix, very elongated ribbons and small un-recrystallized ribbon porphyroclasts. (f) c-axis orientation map (from CIP analysis) of the image in (e) showing the LUT in the lower left corner. (c) CIP-determined c-axis pole figures of the ultramylonite in (f).

Fig. 6 - EBSD analysis of a Y-type ribbon. (a) Orientation map of the ribbon colour-coded according to the inverse pole figure in the lower right corner. Subgrain boundaries are colour-coded as a function of misorientations according to the legend in the upper left corner. (b) Pole figures for

the orientations of [c], <a> and {m} crystallographic directions; (c) Misorientation axis distribution in crystal (upper row) and sample (lower row) coordinate system for both low (2-15°) and high angle misorientations (15-104°). ((d) Scheme of misorientation axis distribution in crystal coordinate system for hexagonal quartz showing the most common slip systems (edge dislocations) for the different misorientation axes (redrawn from Neumann, 2000). (e) Optical microphotographs (crossed polarizers) of the domain mapped in (a) (included in the white box).

Fig. 7 - EBSD orientation imaging and data for an XZa-type ribbon, and included μSZs, in a protomylonite. (a) Orientation map colour-coded according to the inverse pole figure shown in the upper right corner. Boundaries are colour-coded as a function of misorientations according to the same legend in Fig. 6a. (b) Pole figures for the host ribbon showing the orientations of [c], <a> and {r} crystallographic directions. Note the parallelism between one of the {r} crystallographic plane and the μSZ trace (red line). (c) Pole figures ([c], <a> and {m} crystallographic directions) for the recrystallized aggregate along the evolved μSZ δ. (d) Pole figures ([c], <a> and {m} crystallographic directions) for the mature μSZ in the lower part of the map (a). (e) Misorientation axis distributions for low (2-15°) and high (15-104°) misorientation angles and in sample coordinates for the host ribbon. (f) Misorientation axis distributions for low (2-15°), intermediate (15-45°) and high (45-104°) misorientation angles in crystal and sample coordinates for the evolved μSZ δ. (g) Misorientation axis distributions for low (2-15°), intermediate (15-45°) and high (45-104°) misorientation angles in crystal and sample coordinates for the mature μSZ ε. (h) Optical microphotographs (crossed polarizers) of the domain mapped in (a) (included in the red box).

Fig. 8 - EBSD orientation imaging and data of XZb-type ribbon, and included incipient to evolved μSZs. (a) Crystallographic orientation map with inverse pole figure (IPF) for colour-coding (with respect to the X kinematic direction). The ribbon includes 2 incipient μSZs (α and β) with antithetic (left-lateral) sense of shear, and a main synthetic (right-lateral) evolved μSZ (ϕ). (b) Pole figures ([c], {m} and {r} crystallographic orientations) for the host ribbon including the orientations (bold lines) of the μSZs (blue: α; green: β; red: ϕ). (c) Pole figure of the c-axis orientations (one-point-

per-grain) for recrystallized grains in the incipient μSZs α and β, (d) Pole figures of c- and a-axis orientations (one-point-per-grain) for recrystallized grains in the evolved μSZ ϕ. (e) Misorientation axis distributions for low (2-15°) and high (15-104°) misorientations in crystal and sample coordinates for the host ribbon. (f) Misorientation axis distributions (for the misorientation range 2-15°) in crystal and sample coordinates for two selected areas (1) and (2) shown in the orientation map (a). (g) Misorientation axis distributions for low (2-15°), intermediate (15-45°) and high (45-104°) misorientations in crystal and sample coordinates for the evolved μSZ δ. (h) Optical microphotographs (crossed polarizers) of the domain (included in the red box) shown in the EBSD map (a).

Fig. 9 - Misorientation angle distributions (MAD) for correlated (blue curve) and uncorrelated misorientations (red curve). The thin black curve represents the theoretical random distribution for any trigonal point group. M is the misorientation index. (a) Host Y-type ribbon of Fig. 6. (b) Host XZa-type ribbon of Fig. 7. (c) Host XZb-type ribbon of Fig. 8. (d) Host XZa-type ribbon of Fig. 7. (e) Evolved μSZ δ of Fig. 7. (f) Mature μSZ ε of Fig. 7. (g) Evolved μSZ ϕ of Fig. 8. (h) Mature μSZ of Fig. 9. (i) Ultramylonite of Fig. 11.

Fig. 10 - EBSD orientation imaging and data for the quartz ultramylonite. (a) Orientation map colour-coded according to the inverse pole figure shown below. The white solid lines bound domains (I-IV) with a different CPO analysed individually. The dashed white lines encompass quartz ribbon porphyroclasts (b)-(h) c-axis pole figures (1^{st} column), pole figures for low angle misorientations (2^{nd} column) and high angle misorientations (3^{rd} column), and misorientations axis plots in sample coordinates for low (4^{th} column) and high angle misorientations (5^{th} column). In the pole figures, data are reported as one-point-per-grain except for (g) ; (i) Crossed polarizer microphotograph of the ultramylonite (red box indicate the analysed area).

1063

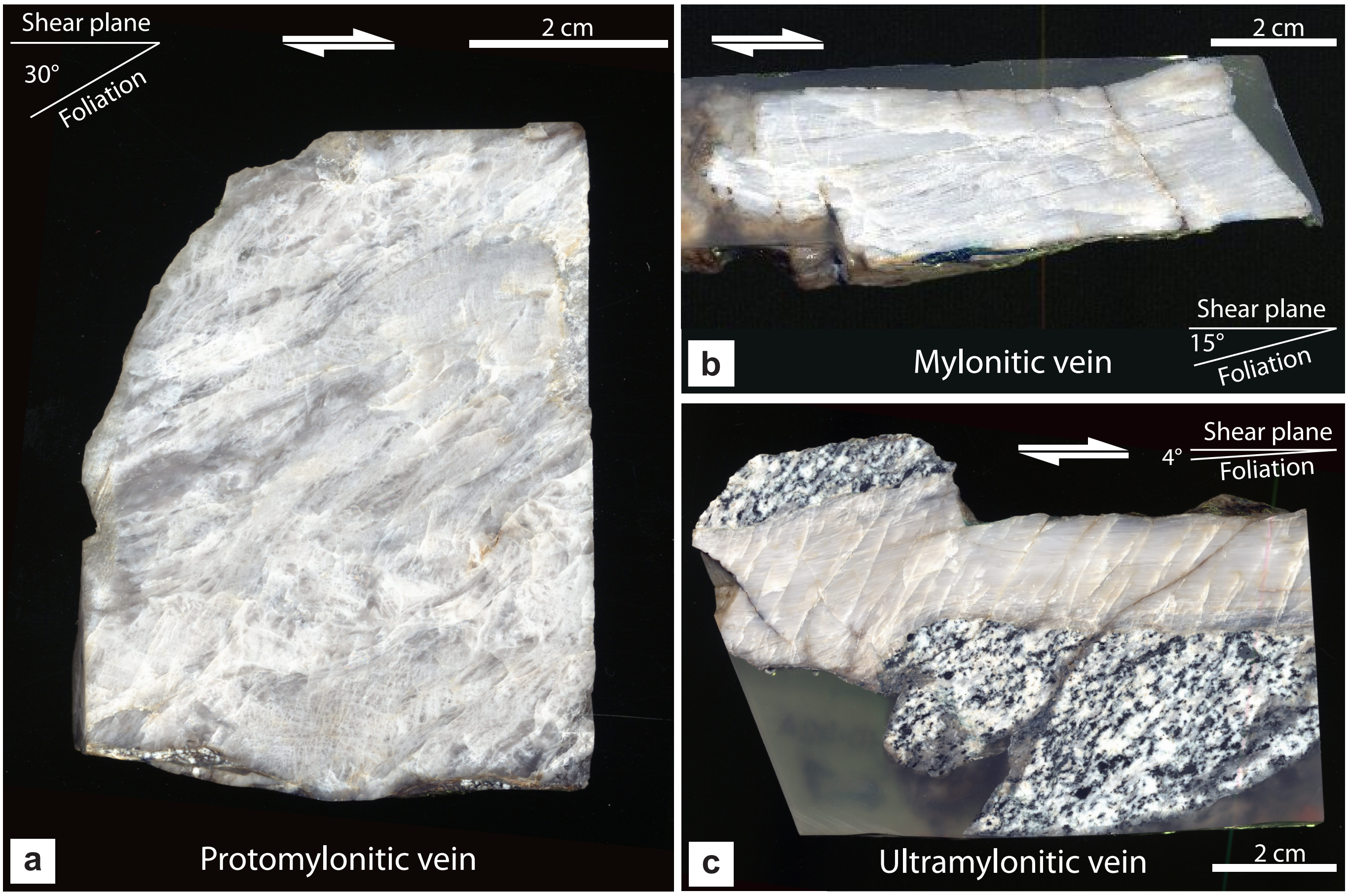
Shear plane
30°
Foliation
2 cm
a
Protomylonitic vein
2 cm
Shear plane
15°
Foliation
b
Mylonitic vein
Shear plane
4°
Foliation
c
Ultramylonitic vein
2 cm

Figure 1

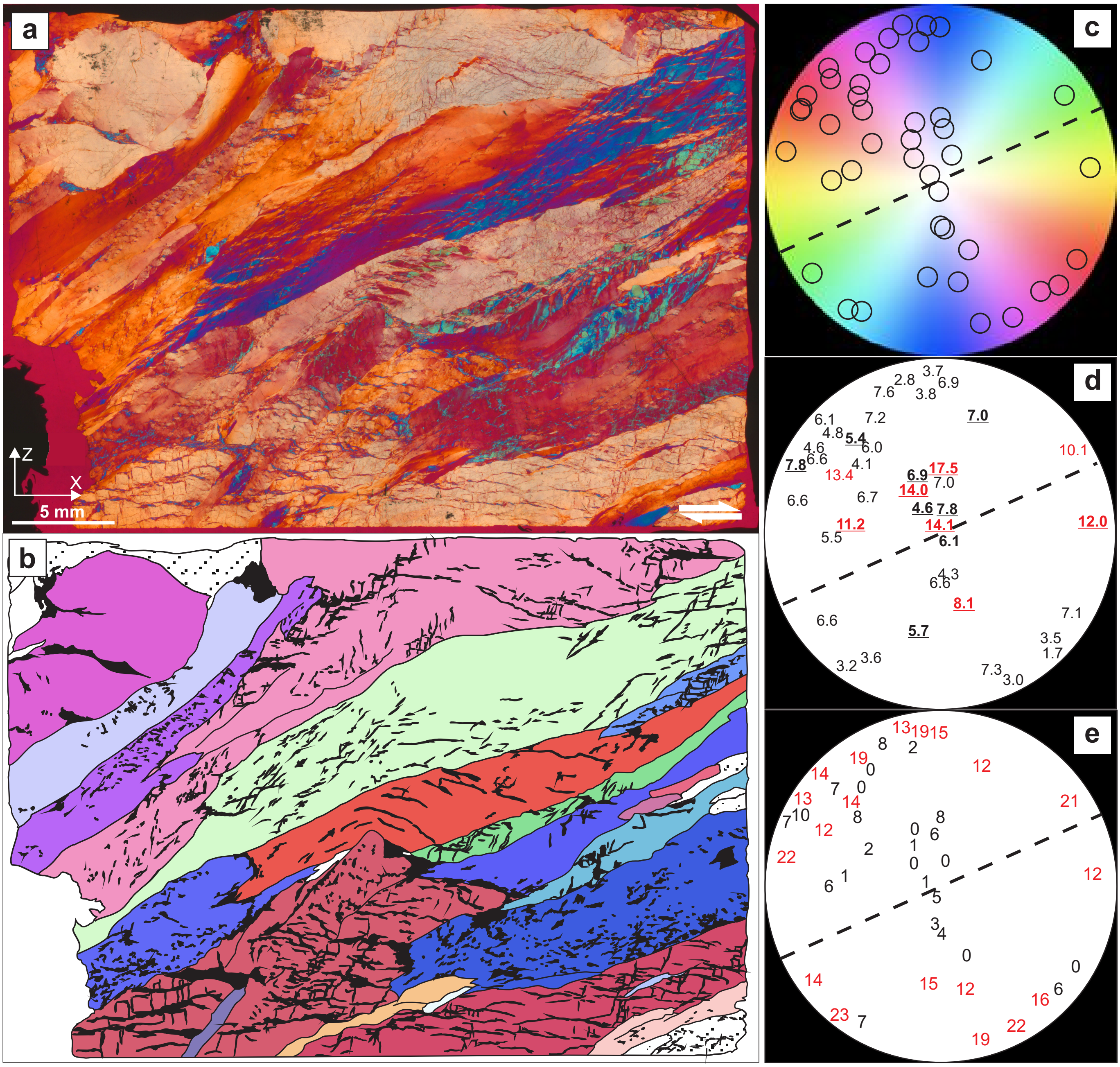
a
Z
X
5 mm
b
c
d
3.7
2.8
6.9
7.6
3.8
6.1
7.2
7.0
4.8
5.4
6.0
4.6
10.1
7.8
6.6
4.1
17.5
6.9
13.4
7.0
14.0
6.6
6.7
4.6
7.8
11.2
14.1
12.0
5.5
6.1
4.3
6.6
8.1
7.1
6.6
5.7
3.5
1.7
3.6
3.2
7.3
3.0
e
13
19
15
8
2
19
0
12
14
7
0
13
14
21
7
10
8
8
12
0
6
2
1
22
0
0
12
6
1
1
5
3
4
0
14
0
15
12
6
16
23
7
22
19

Figure 2

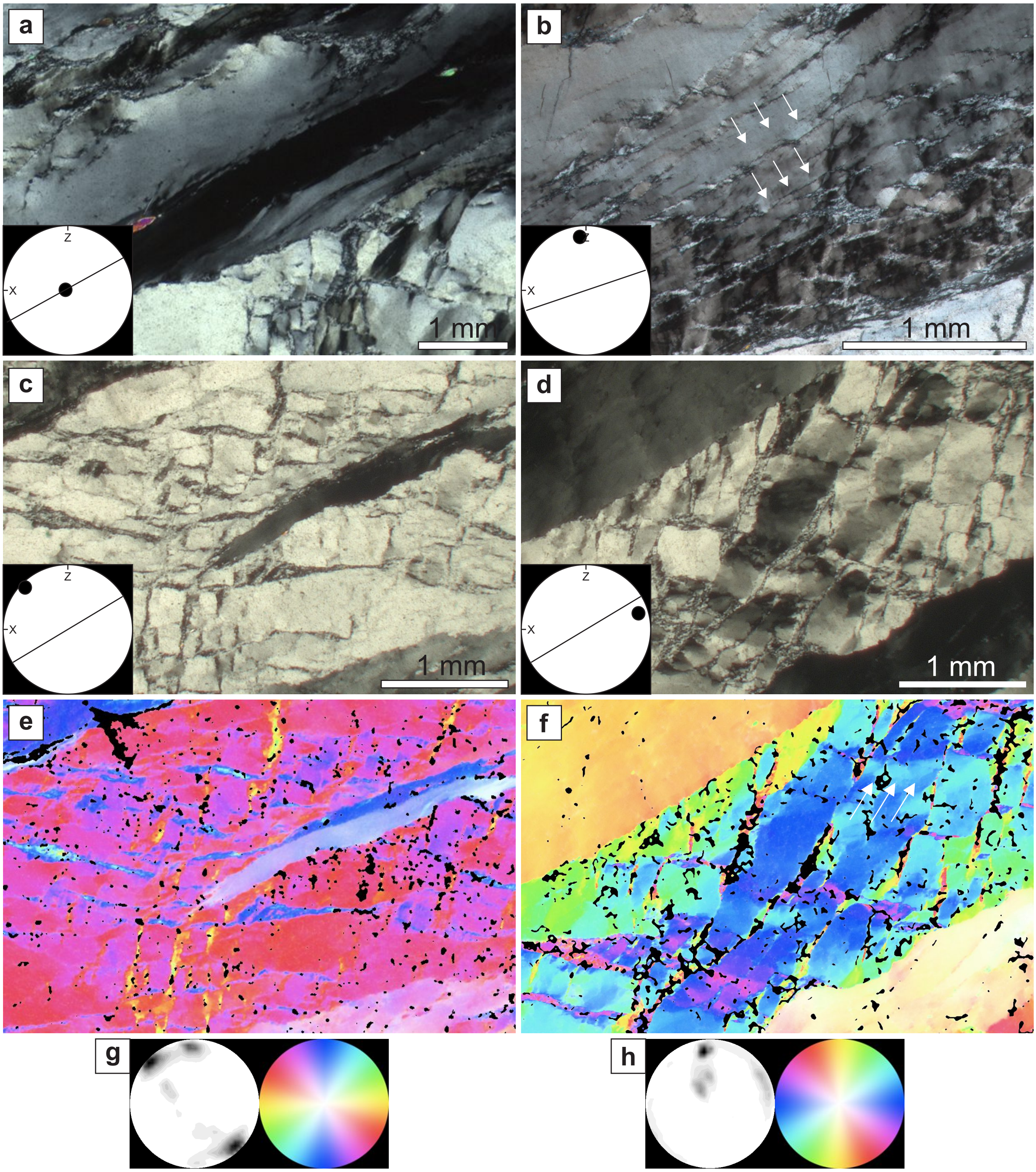

Figure 3

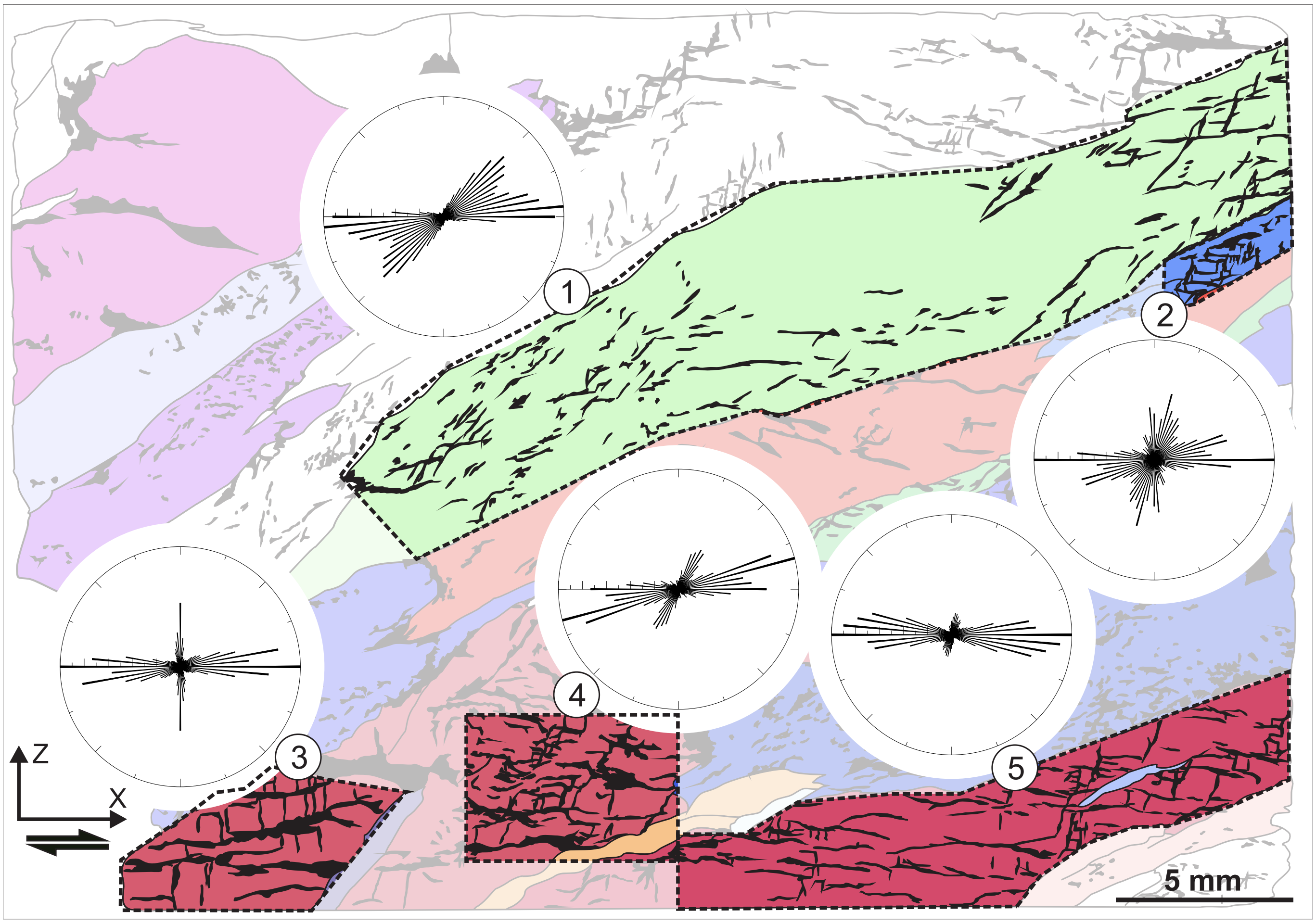

Figure 4

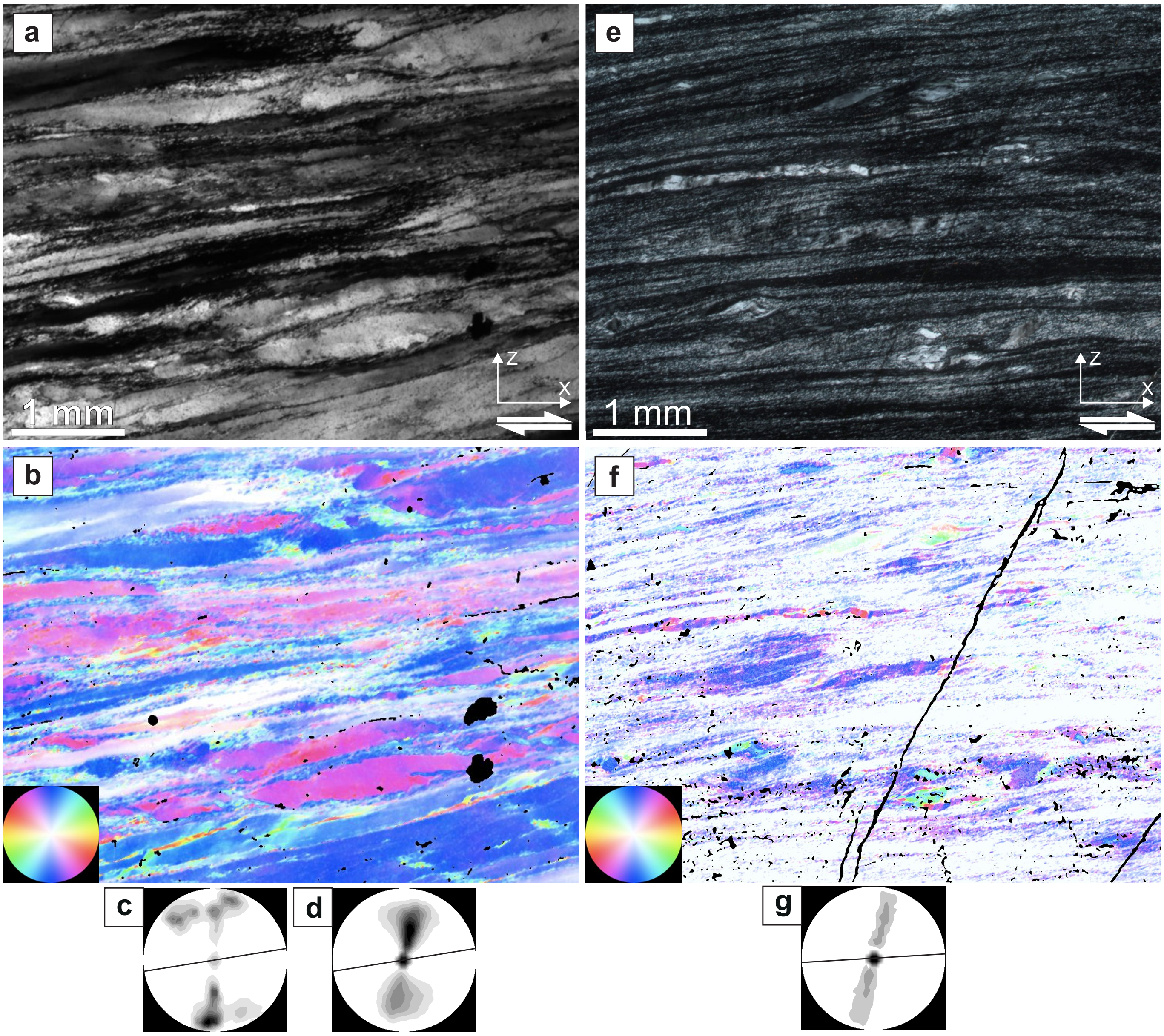

Figure 5

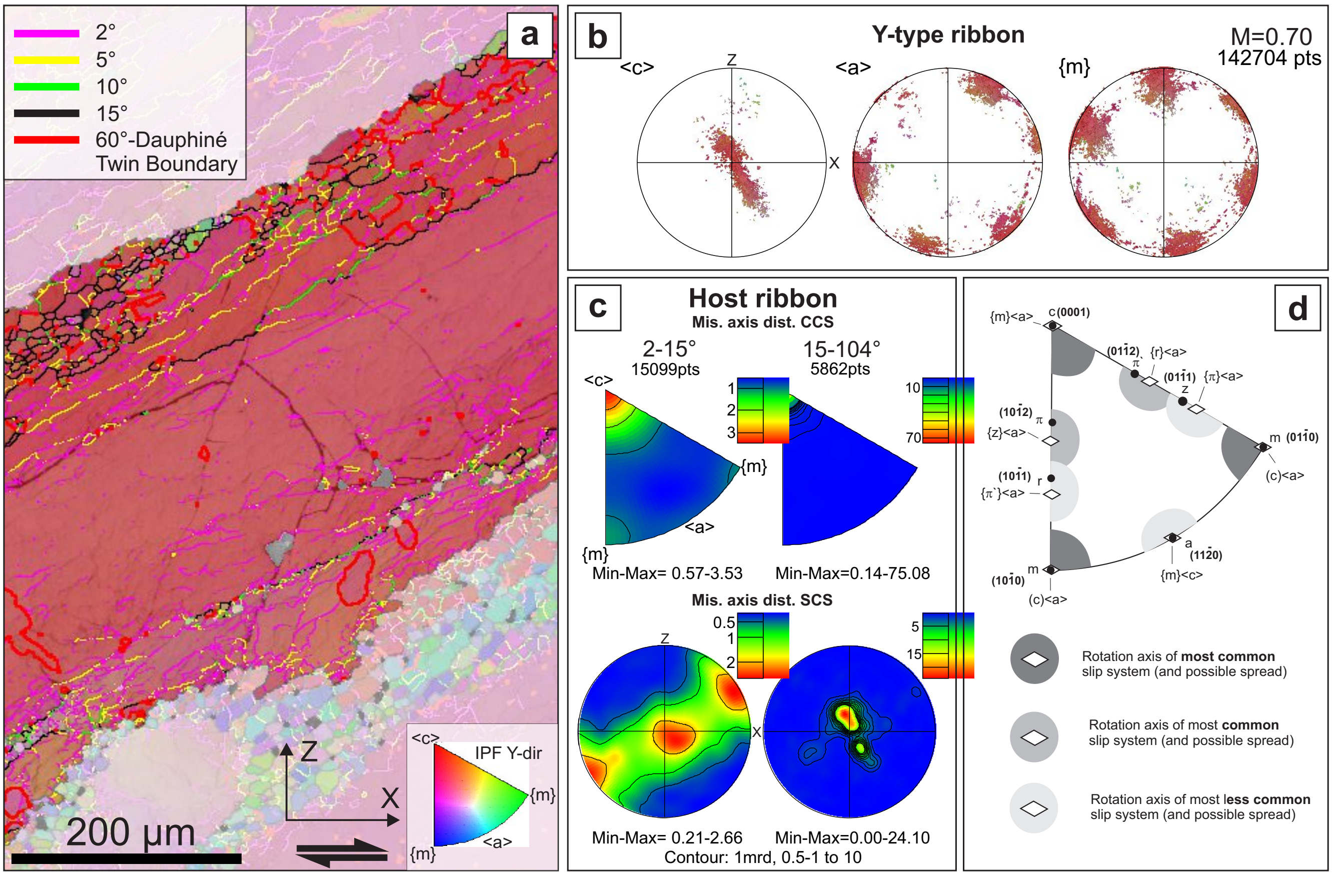

a
2°
5°
10°
15°
60°-Dauphiné Twin Boundary
200 µm
Z
X
IPF Y-dir
<c>
{m}
<a>
b
Y-type ribbon
M=0.70
142704 pts
<c>
<a>
{m}
c
Host ribbon
Mis. axis dist. CCS
2-15°
15099pts
15-104°
5862pts
Min-Max= 0.57-3.53
Min-Max=0.14-75.08
Mis. axis dist. SCS
Min-Max= 0.21-2.66
Min-Max=0.00-24.10
Contour: 1mrd, 0.5-1 to 10
d
Rotation axis of most common slip system (and possible spread)
Rotation axis of most common slip system (and possible spread)
Rotation axis of most less common slip system (and possible spread)

Figure 6

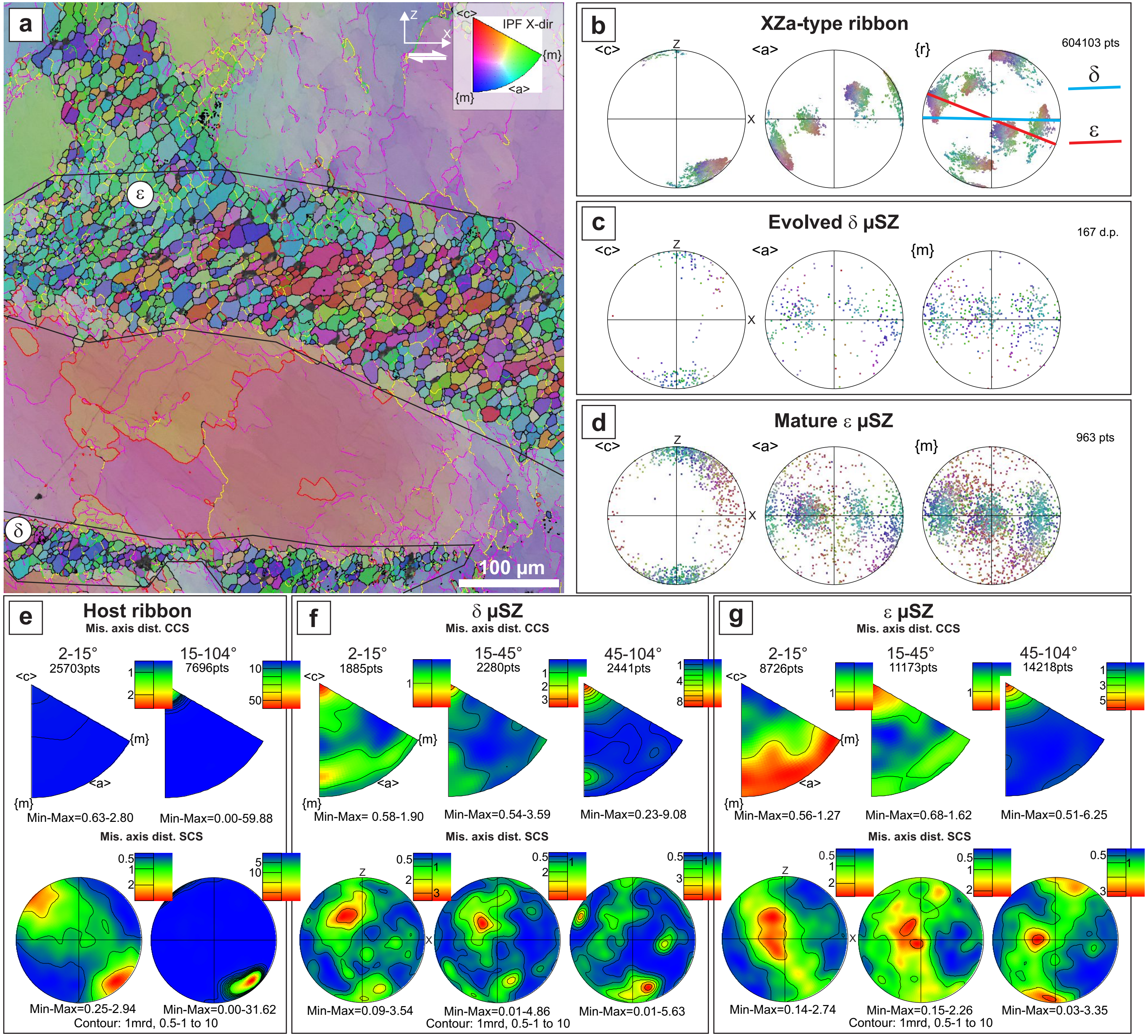
a
IPF X-dir
ε
δ
100 μm
b
XZa-type ribbon
604103 pts
<c>
<a>
{r}
δ
ε
c
Evolved δ μSZ
167 d.p.
d
Mature ε μSZ
963 pts
e
Host ribbon
Mis. axis dist. CCS
2-15°
25703pts
15-104°
7696pts
Min-Max=0.63-2.80
Min-Max=0.00-59.88
Mis. axis dist. SCS
Min-Max=0.25-2.94
Min-Max=0.00-31.62
Contour: 1mrd, 0.5-1 to 10
f
δ μSZ
Mis. axis dist. CCS
2-15°
1885pts
15-45°
2280pts
45-104°
2441pts
Min-Max= 0.58-1.90
Min-Max=0.54-3.59
Min-Max=0.23-9.08
Mis. axis dist. SCS
Min-Max=0.09-3.54
Min-Max=0.01-4.86
Min-Max=0.01-5.63
Contour: 1mrd, 0.5-1 to 10
g
ε μSZ
Mis. axis dist. CCS
2-15°
8726pts
15-45°
11173pts
45-104°
14218pts
Min-Max=0.56-1.27
Min-Max=0.68-1.62
Min-Max=0.51-6.25
Mis. axis dist. SCS
Min-Max=0.14-2.74
Min-Max=0.15-2.26
Min-Max=0.03-3.35
Contour: 1mrd, 0.5-1 to 10

Figure 7

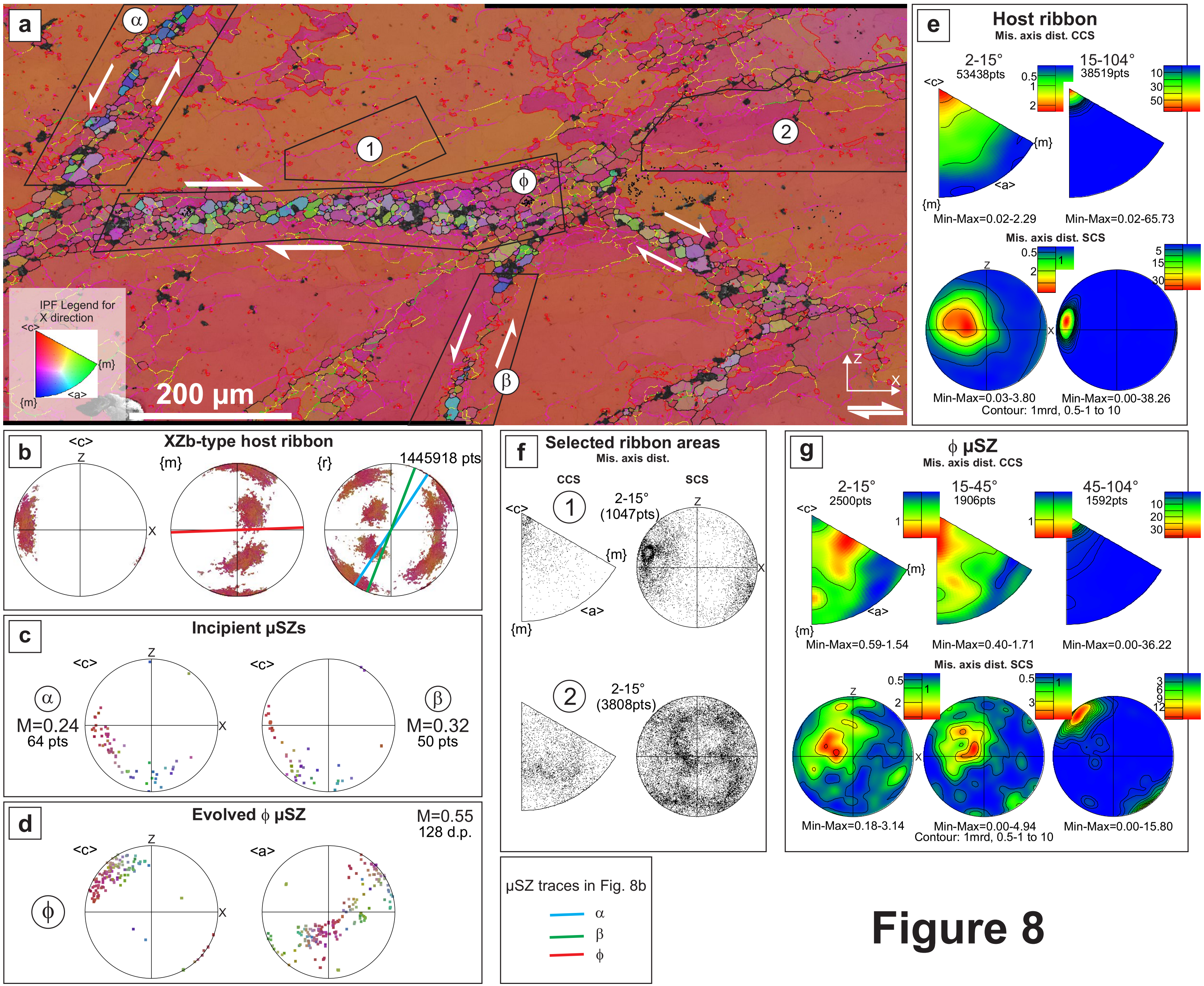

a
α
β
ϕ
1
2
IPF Legend for X direction
<c>
{m}
<a>
200 µm
Z
X
e
Host ribbon
Mis. axis dist. CCS
2-15°
53438pts
15-104°
38519pts
Min-Max=0.02-2.29
Min-Max=0.02-65.73
Mis. axis dist. SCS
Min-Max=0.03-3.80
Min-Max=0.00-38.26
Contour: 1mrd, 0.5-1 to 10
b
XZb-type host ribbon
<c>
{m}
{r}
1445918 pts
c
Incipient µSZs
M=0.24
64 pts
M=0.32
50 pts
d
Evolved ϕ µSZ
M=0.55
128 d.p.
<a>
f
Selected ribbon areas
Mis. axis dist.
CCS
SCS
2-15°
(1047pts)
(3808pts)
g
ϕ µSZ
Mis. axis dist. CCS
2-15°
2500pts
15-45°
1906pts
45-104°
1592pts
Min-Max=0.59-1.54
Min-Max=0.40-1.71
Min-Max=0.00-36.22
Mis. axis dist. SCS
Min-Max=0.18-3.14
Min-Max=0.00-4.94
Contour: 1mrd, 0.5-1 to 10
Min-Max=0.00-15.80
µSZ traces in Fig. 8b

Figure 8

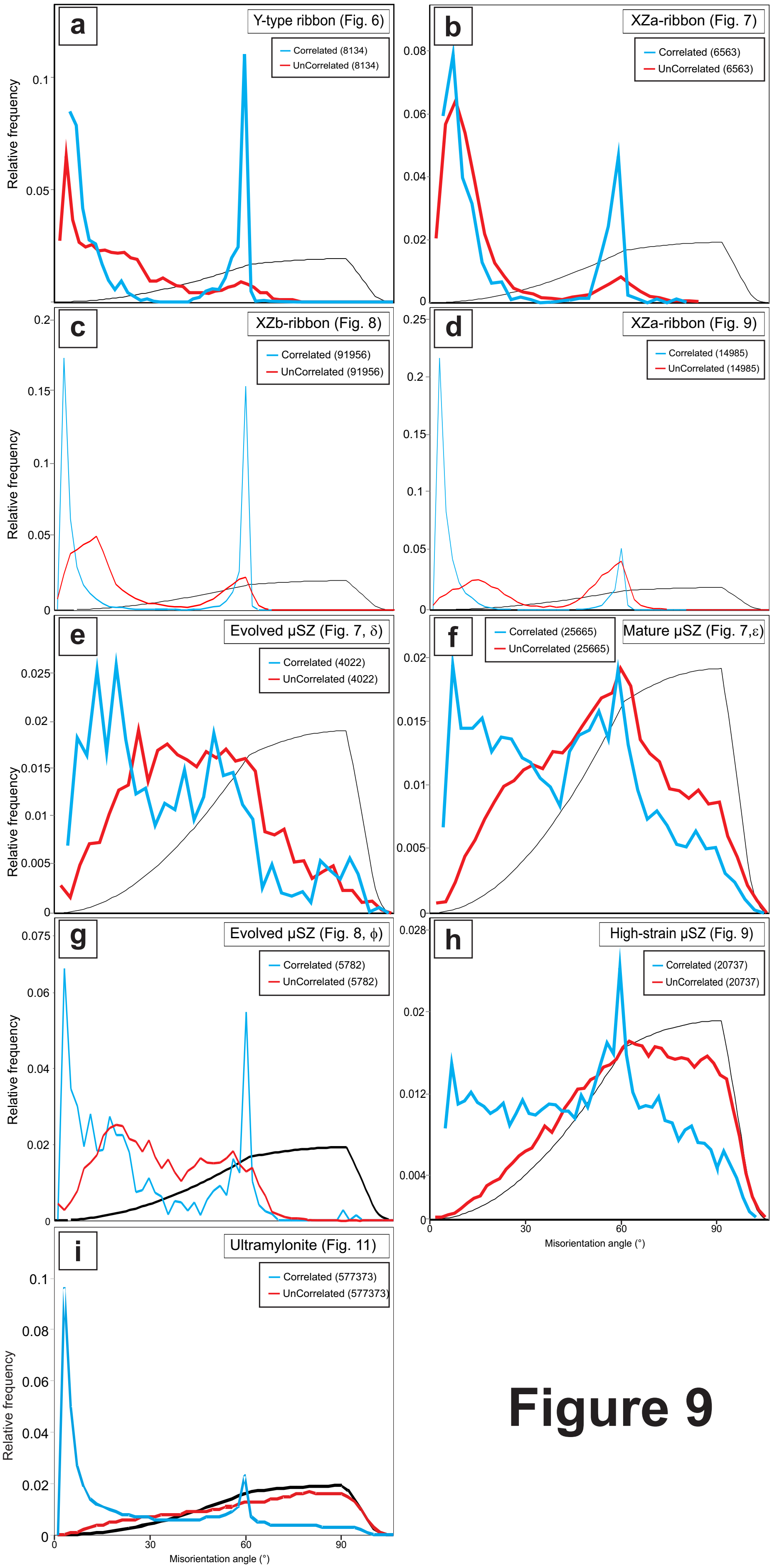
a
Y-type ribbon (Fig. 6)
Correlated (8134)
UnCorrelated (8134)
b
XZa-ribbon (Fig. 7)
Correlated (6563)
UnCorrelated (6563)
c
XZb-ribbon (Fig. 8)
Correlated (91956)
UnCorrelated (91956)
d
XZa-ribbon (Fig. 9)
Correlated (14985)
UnCorrelated (14985)
e
Evolved μSZ (Fig. 7, δ)
Correlated (4022)
UnCorrelated (4022)
f
Mature μSZ (Fig. 7,ε)
Correlated (25665)
UnCorrelated (25665)
g
Evolved μSZ (Fig. 8, ϕ)
Correlated (5782)
UnCorrelated (5782)
h
High-strain μSZ (Fig. 9)
Correlated (20737)
UnCorrelated (20737)
i
Ultramylonite (Fig. 11)
Correlated (577373)
UnCorrelated (577373)
Relative frequency
Misorientation angle (°)
0
30
60
90

Figure 9

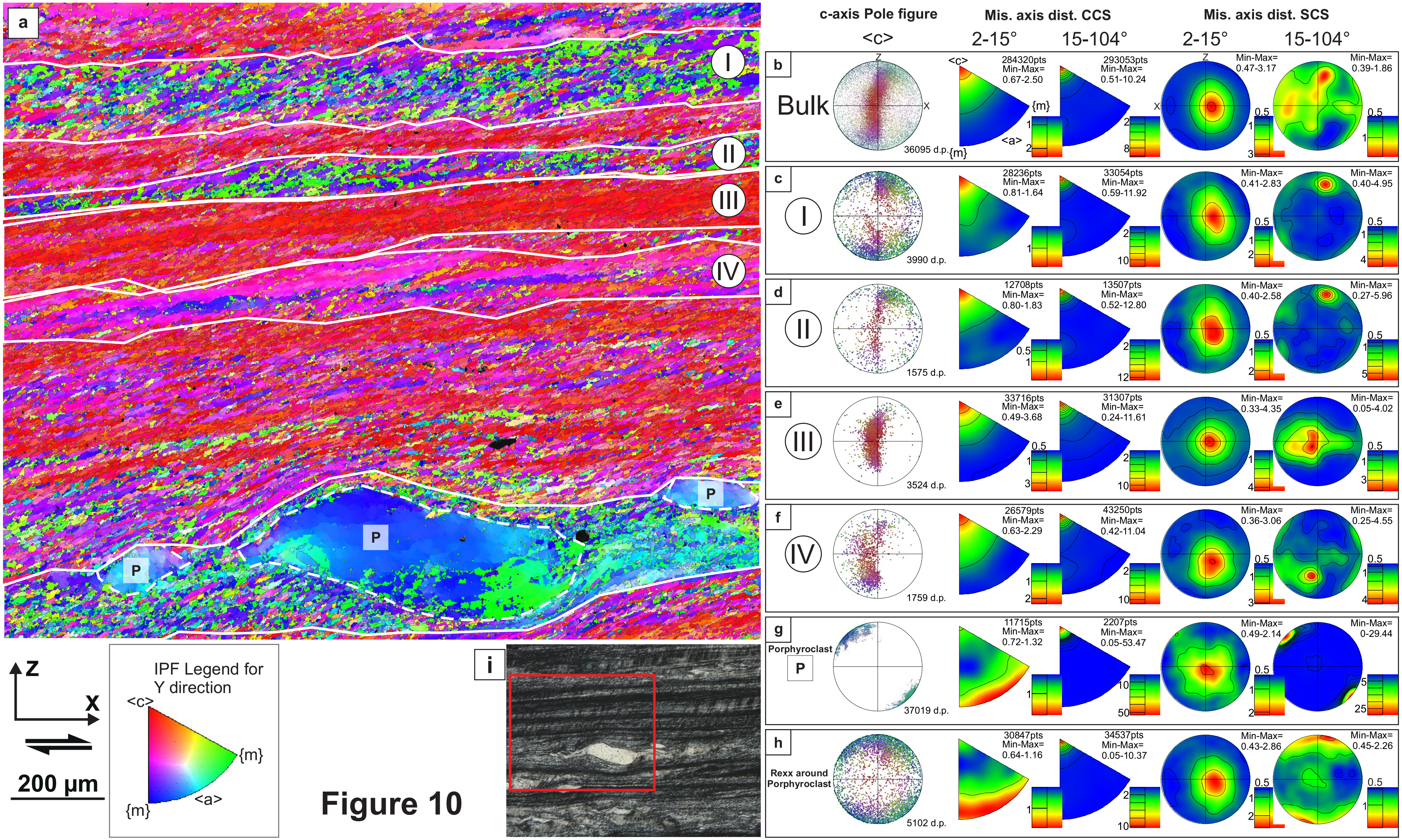

a
I
II
III
IV
P
P
P
P
Z
X
200 µm
IPF Legend for Y direction
<c>
{m}
{m}
<a>
i
c-axis Pole figure
<c>
Mis. axis dist. CCS
2-15°
15-104°
Mis. axis dist. SCS
2-15°
15-104°
b
Bulk
36095 d.p.
284320pts Min-Max= 0.67-2.50
293053pts Min-Max= 0.51-10.24
Min-Max= 0.47-3.17
Min-Max= 0.39-1.86
c
I
3990 d.p.
28236pts Min-Max= 0.81-1.64
33054pts Min-Max= 0.59-11.92
Min-Max= 0.41-2.83
Min-Max= 0.40-4.95
d
II
1575 d.p.
12708pts Min-Max= 0.80-1.83
13507pts Min-Max= 0.52-12.80
Min-Max= 0.40-2.58
Min-Max= 0.27-5.96
e
III
3524 d.p.
33716pts Min-Max= 0.49-3.68
31307pts Min-Max= 0.24-11.61
Min-Max= 0.33-4.35
Min-Max= 0.05-4.02
f
IV
1759 d.p.
26579pts Min-Max= 0.63-2.29
43250pts Min-Max= 0.42-11.04
Min-Max= 0.36-3.06
Min-Max= 0.25-4.55
g
Porphyroclast
P
37019 d.p.
11715pts Min-Max= 0.72-1.32
2207pts Min-Max= 0.05-53.47
Min-Max= 0.49-2.14
Min-Max= 0-29.44
h
Rexx around Porphyroclast
5102 d.p.
30847pts Min-Max= 0.64-1.16
34537pts Min-Max= 0.05-10.37
Min-Max= 0.43-2.86
Min-Max= 0.45-2.26

Figure 10

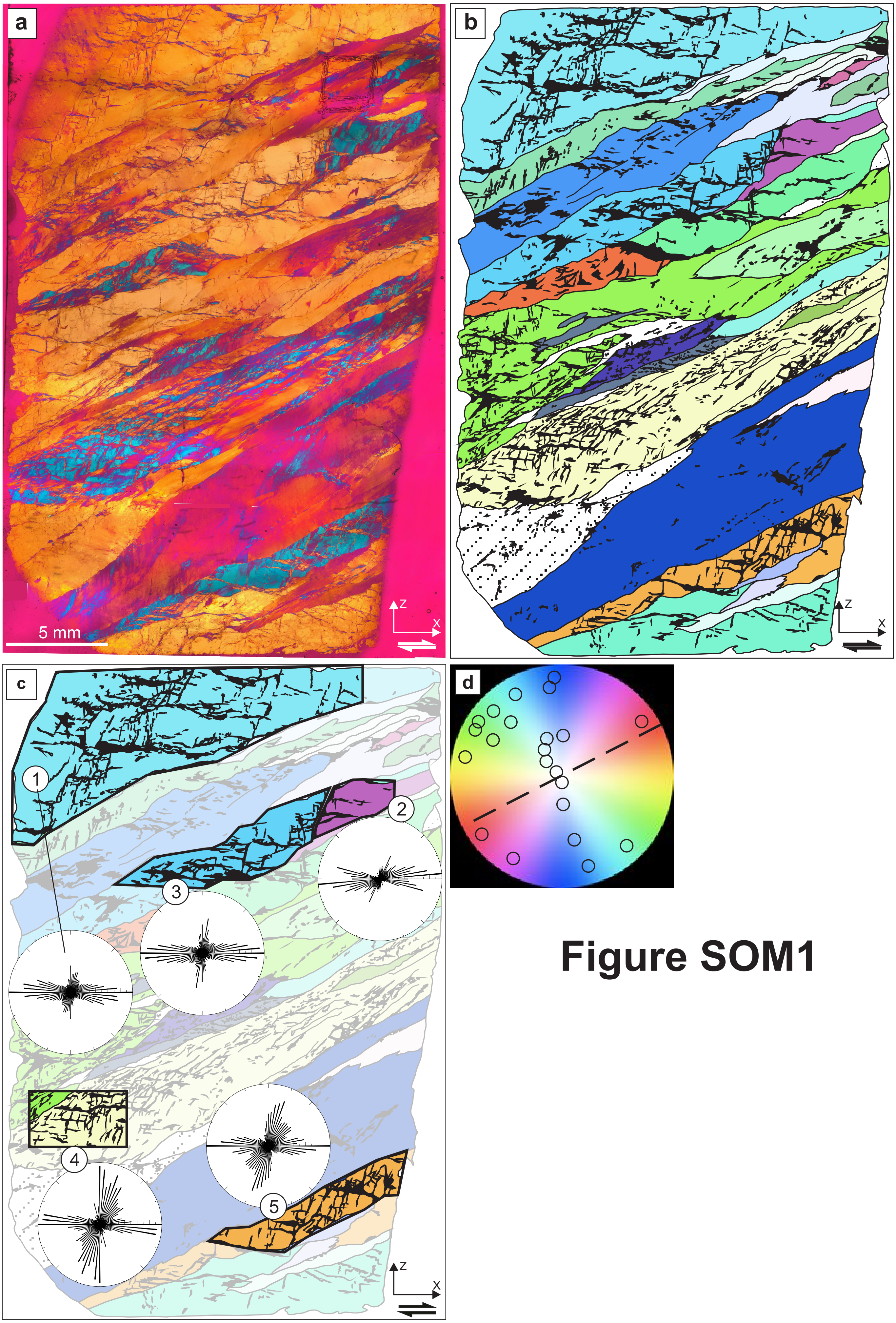

Figure SOM1

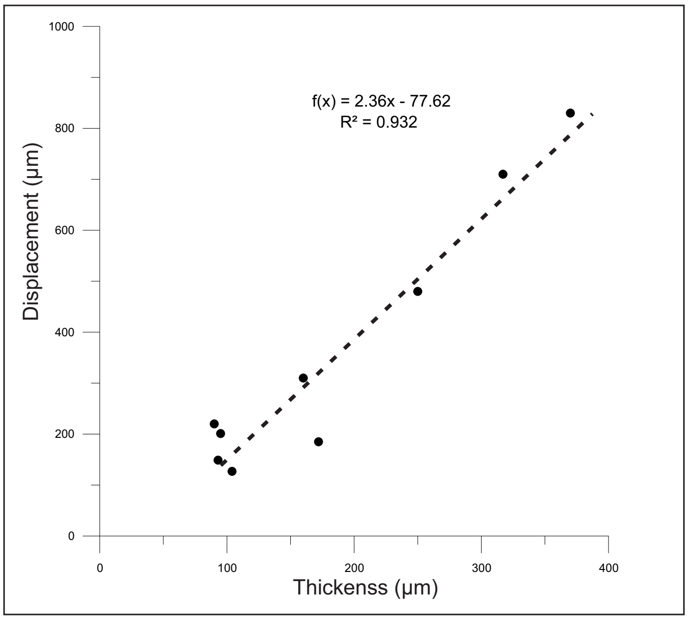

f(x) = 2.36x - 77.62
R² = 0.932
Displacement (µm)
Thickenss (µm)
1000
800
600
400
200
0
0
100
200
300
400

Figure SOM2

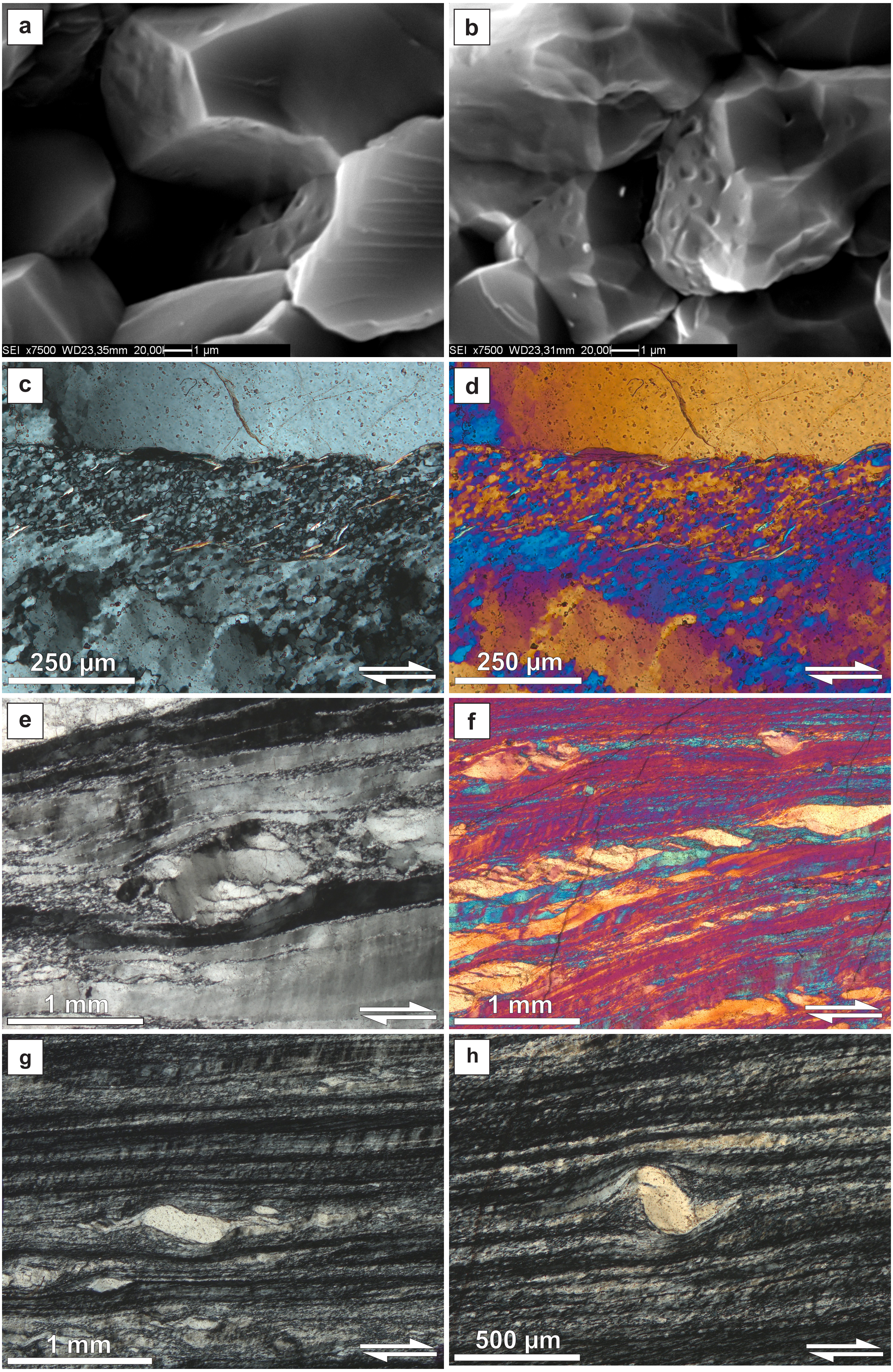
a
b
SEI x7500 WD23,35mm 20,00 1 µm
SEI x7500 WD23,31mm 20,00 1 µm
c
d
250 µm
250 µm
e
f
1 mm
1 mm
g
h
1 mm
500 µm

Figure SOM3

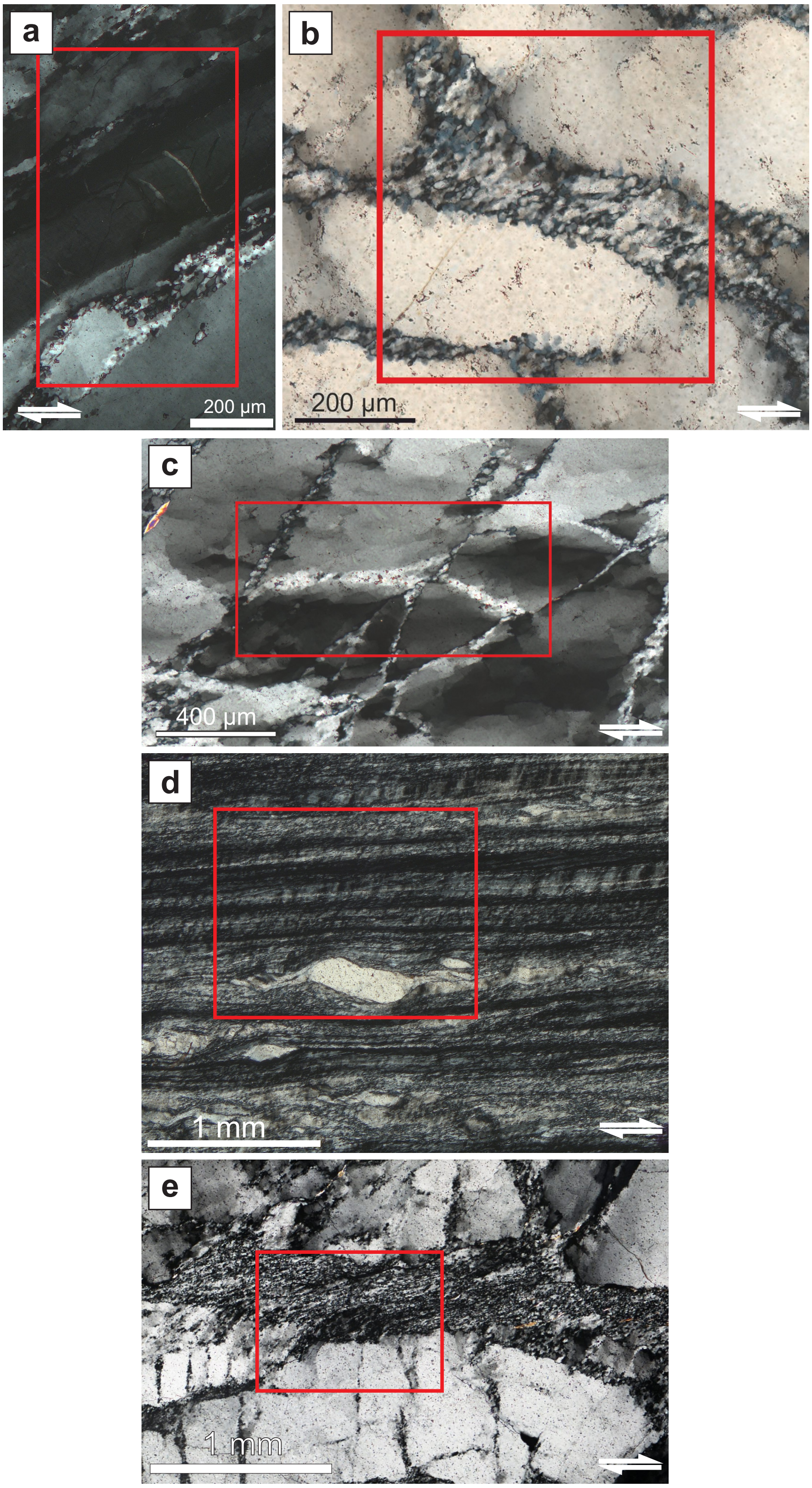

Figure SOM4

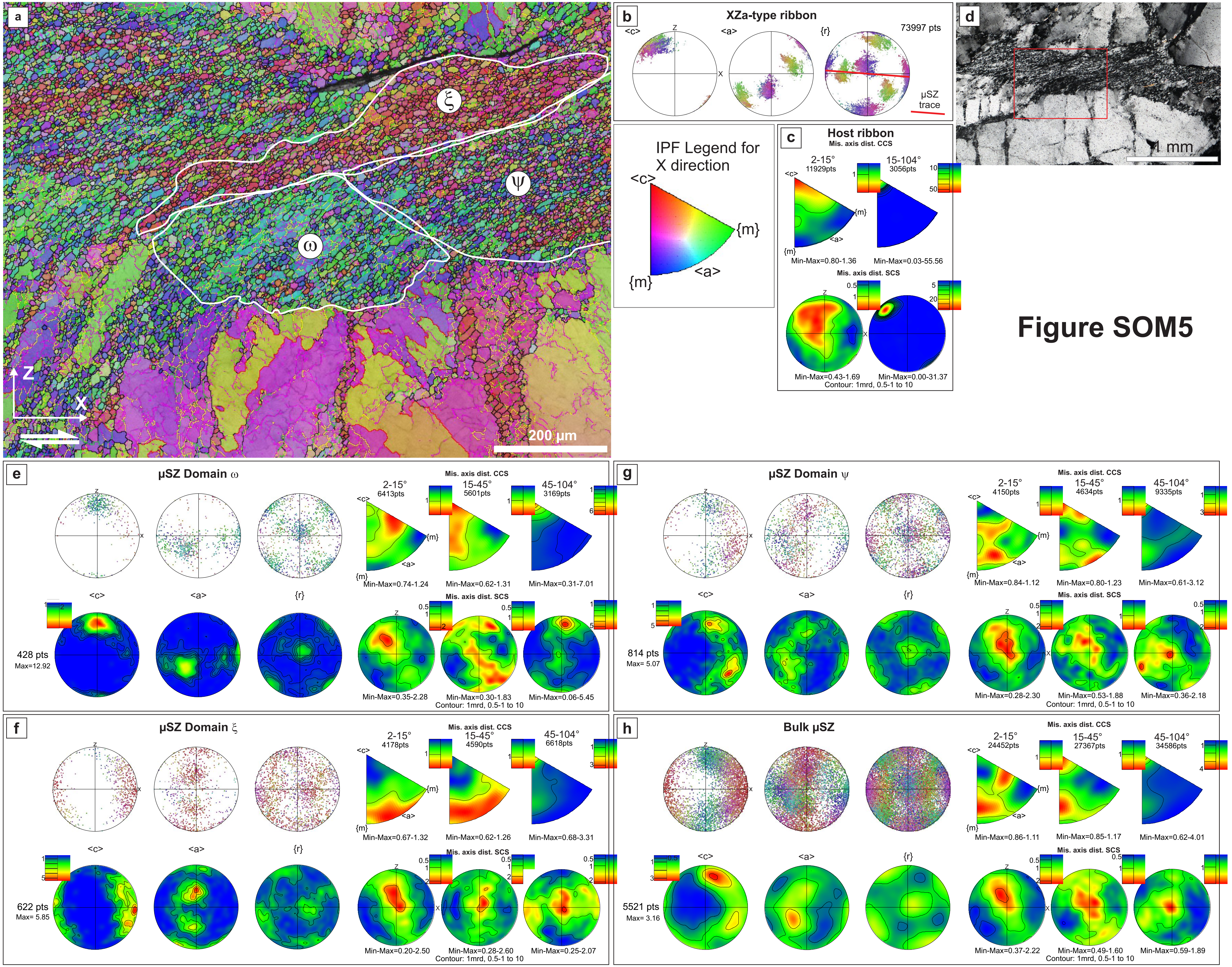

a
ξ
ψ
ω
Z
X
200 µm
b
XZa-type ribbon
<c>
<a>
{r}
73997 pts
µSZ trace
IPF Legend for X direction
c
Host ribbon
Mis. axis dist. CCS
2-15°
11929pts
15-104°
3056pts
Min-Max=0.80-1.36
Min-Max=0.03-55.56
Mis. axis dist. SCS
Min-Max=0.43-1.69
Min-Max=0.00-31.37
Contour: 1mrd, 0.5-1 to 10
d
1 mm
e
µSZ Domain ω
2-15°
6413pts
15-45°
5601pts
45-104°
3169pts
Min-Max=0.74-1.24
Min-Max=0.62-1.31
Min-Max=0.31-7.01
428 pts
Max=12.92
Min-Max=0.35-2.28
Min-Max=0.30-1.83
Min-Max=0.06-5.45
Contour: 1mrd, 0.5-1 to 10
g
µSZ Domain ψ
2-15°
4150pts
15-45°
4634pts
45-104°
9335pts
Min-Max=0.84-1.12
Min-Max=0.80-1.23
Min-Max=0.61-3.12
814 pts
Max= 5.07
Min-Max=0.28-2.30
Min-Max=0.53-1.88
Min-Max=0.36-2.18
Contour: 1mrd, 0.5-1 to 10
f
µSZ Domain ξ
2-15°
4178pts
15-45°
4590pts
45-104°
6618pts
Min-Max=0.67-1.32
Min-Max=0.62-1.26
Min-Max=0.68-3.31
622 pts
Max= 5.85
Min-Max=0.20-2.50
Min-Max=0.28-2.60
Min-Max=0.25-2.07
Contour: 1mrd, 0.5-1 to 10
h
Bulk µSZ
2-15°
24452pts
15-45°
27367pts
45-104°
34586pts
Min-Max=0.86-1.11
Min-Max=0.85-1.17
Min-Max=0.62-4.01
5521 pts
Max= 3.16
Min-Max=0.37-2.22
Min-Max=0.49-1.60
Min-Max=0.59-1.89
Contour: 1mrd, 0.5-1 to 10

Figure SOM5

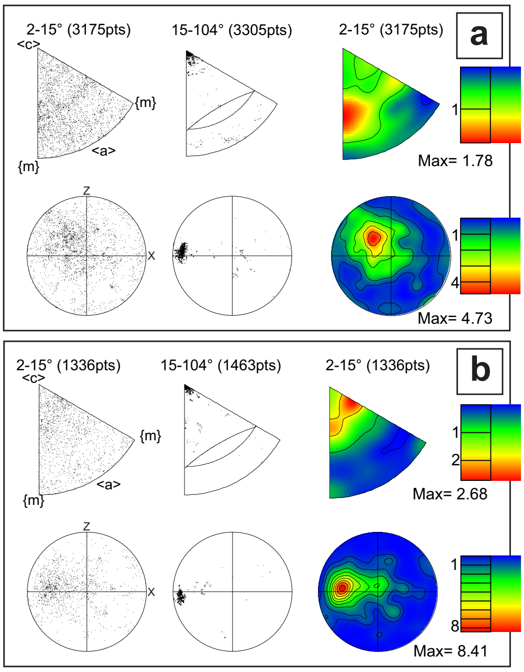

a
2-15° (3175pts)
15-104° (3305pts)
2-15° (3175pts)
<c>
{m}
<a>
{m}
Max= 1.78
Z
X
Max= 4.73
b
2-15° (1336pts)
15-104° (1463pts)
2-15° (1336pts)
Max= 2.68
Max= 8.41

Figure SOM6

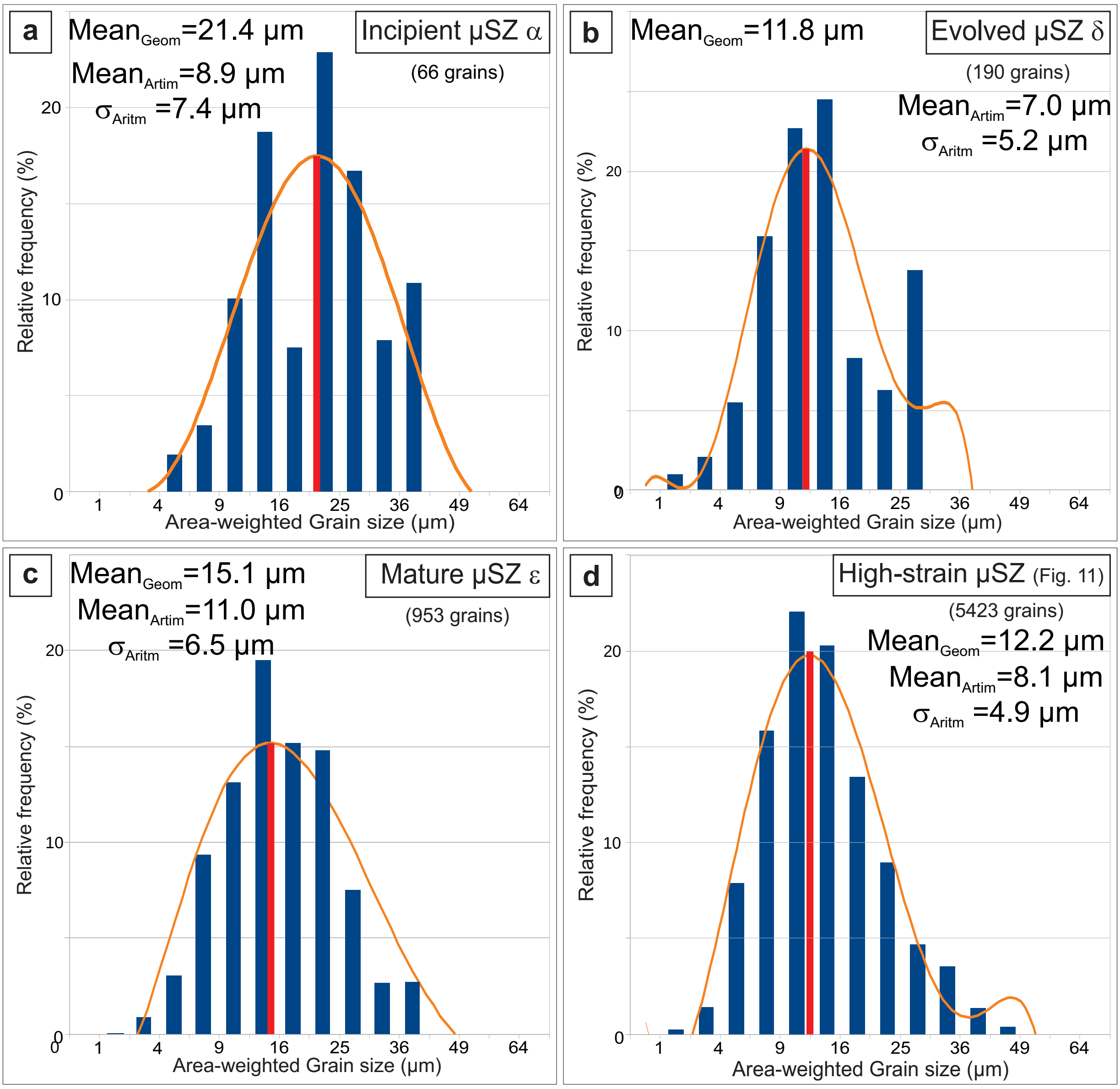

a
Mean$_{Geom}$=21.4 µm
Mean$_{Artim}$=8.9 µm
σ$_{Aritm}$ =7.4 µm
Incipient µSZ α
(66 grains)
Relative frequency (%)
Area-weighted Grain size (µm)
b
Mean$_{Geom}$=11.8 µm
Evolved µSZ δ
(190 grains)
Mean$_{Artim}$=7.0 µm
σ$_{Aritm}$ =5.2 µm
Relative frequency (%)
Area-weighted Grain size (µm)
c
Mean$_{Geom}$=15.1 µm
Mean$_{Artim}$=11.0 µm
σ$_{Aritm}$ =6.5 µm
Mature µSZ ε
(953 grains)
Relative frequency (%)
Area-weighted Grain size (µm)
d
High-strain µSZ (Fig. 11)
(5423 grains)
Mean$_{Geom}$=12.2 µm
Mean$_{Artim}$=8.1 µm
σ$_{Aritm}$ =4.9 µm
Relative frequency (%)
Area-weighted Grain size (µm)

Figure SOM7

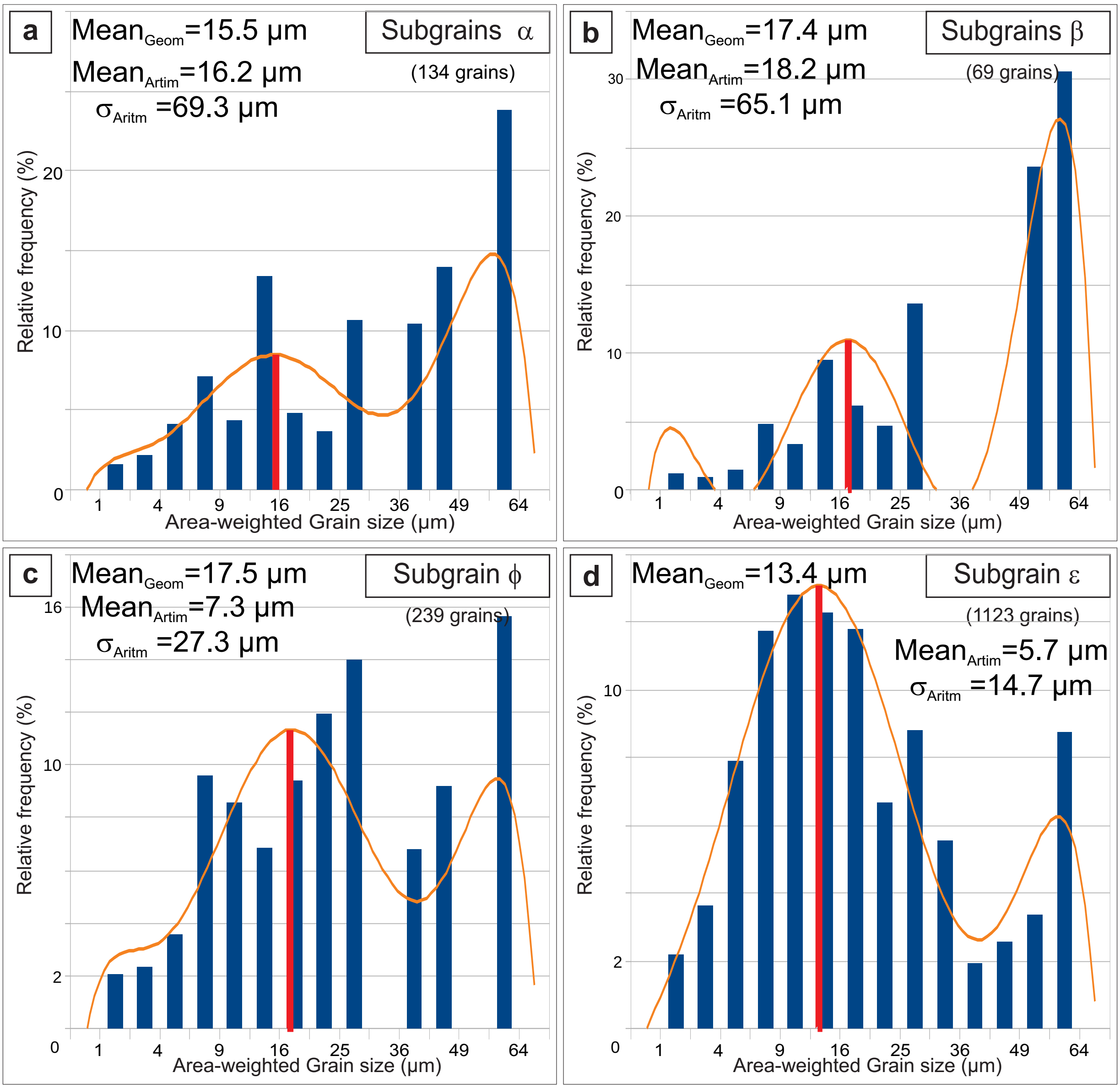
a
Mean_Geom=15.5 µm
Mean_Artim=16.2 µm
σ_Aritm =69.3 µm
Subgrains α
(134 grains)
Relative frequency (%)
Area-weighted Grain size (µm)
b
Mean_Geom=17.4 µm
Mean_Artim=18.2 µm
σ_Aritm =65.1 µm
Subgrains β
(69 grains)
Relative frequency (%)
Area-weighted Grain size (µm)
c
Mean_Geom=17.5 µm
Mean_Artim=7.3 µm
σ_Aritm =27.3 µm
Subgrain ϕ
(239 grains)
Relative frequency (%)
Area-weighted Grain size (µm)
d
Mean_Geom=13.4 µm
Subgrain ε
(1123 grains)
Mean_Artim=5.7 µm
σ_Aritm =14.7 µm
Relative frequency (%)
Area-weighted Grain size (µm)

Figure SOM8

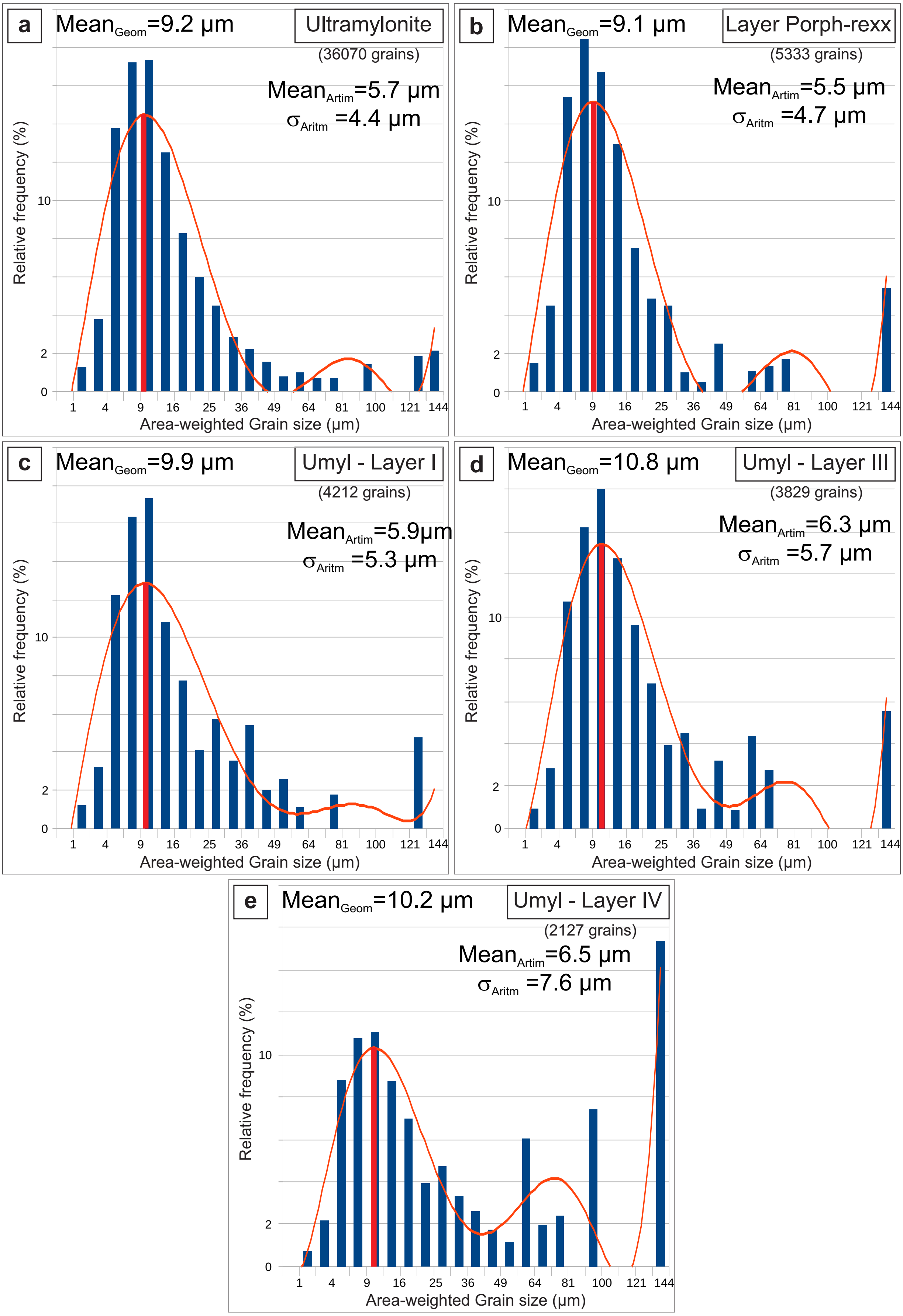
a
Mean$_{Geom}$=9.2 µm
Ultramylonite
(36070 grains)
Mean$_{Artim}$=5.7 µm
σ_{Aritm} =4.4 µm
Relative frequency (%)
Area-weighted Grain size (µm)
b
Mean$_{Geom}$=9.1 µm
Layer Porph-rexx
(5333 grains)
Mean$_{Artim}$=5.5 µm
σ_{Aritm} =4.7 µm
c
Mean$_{Geom}$=9.9 µm
Umyl - Layer I
(4212 grains)
Mean$_{Artim}$=5.9µm
σ_{Aritm} =5.3 µm
d
Mean$_{Geom}$=10.8 µm
Umyl - Layer III
(3829 grains)
Mean$_{Artim}$=6.3 µm
σ_{Aritm} =5.7 µm
e
Mean$_{Geom}$=10.2 µm
Umyl - Layer IV
(2127 grains)
Mean$_{Artim}$=6.5 µm
σ_{Aritm} =7.6 µm
0
2
10
1
4
9
16
25
36
49
64
81
100
121
144

Figure SOM9

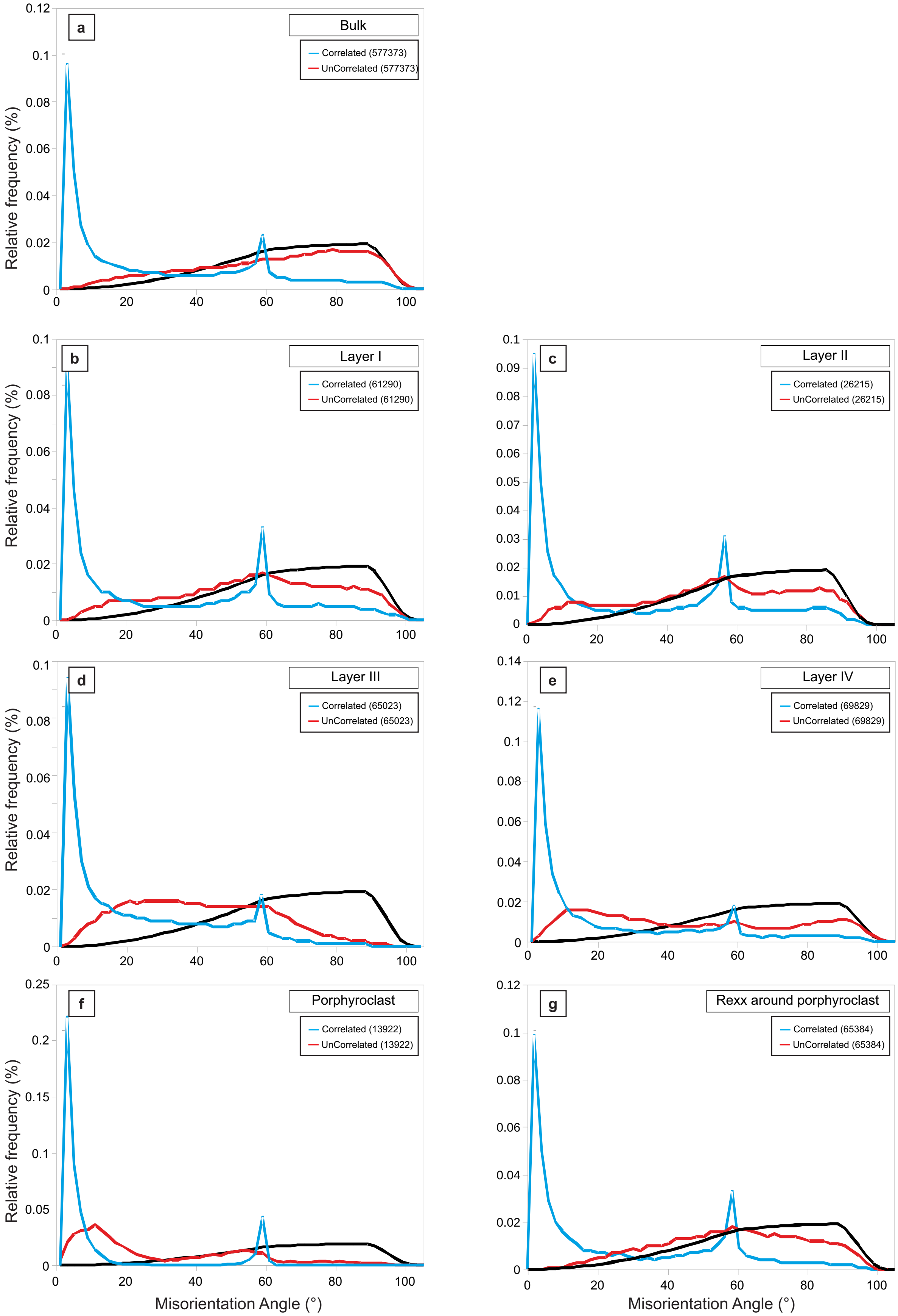

Figure SOM10

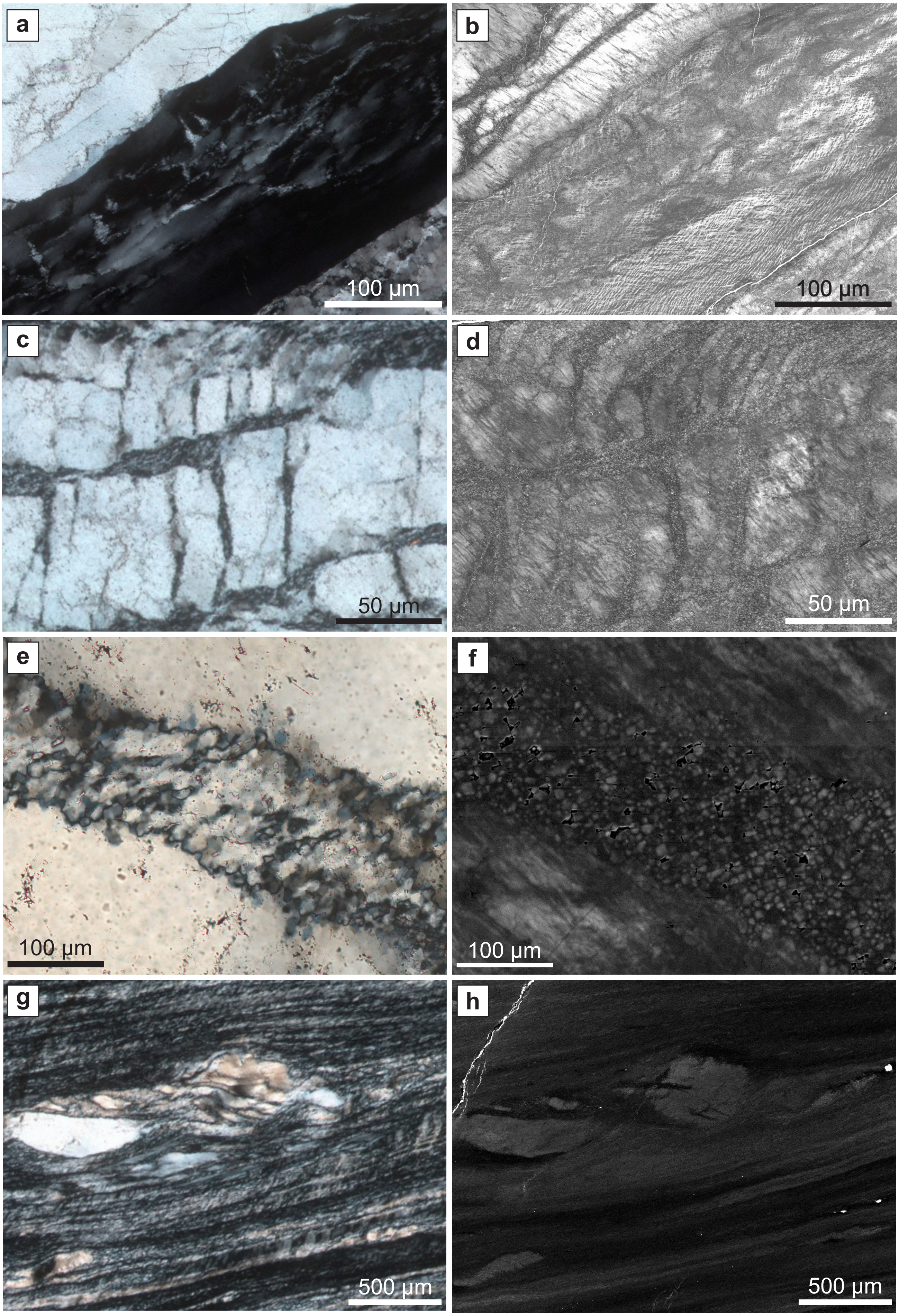

Figure SOM11

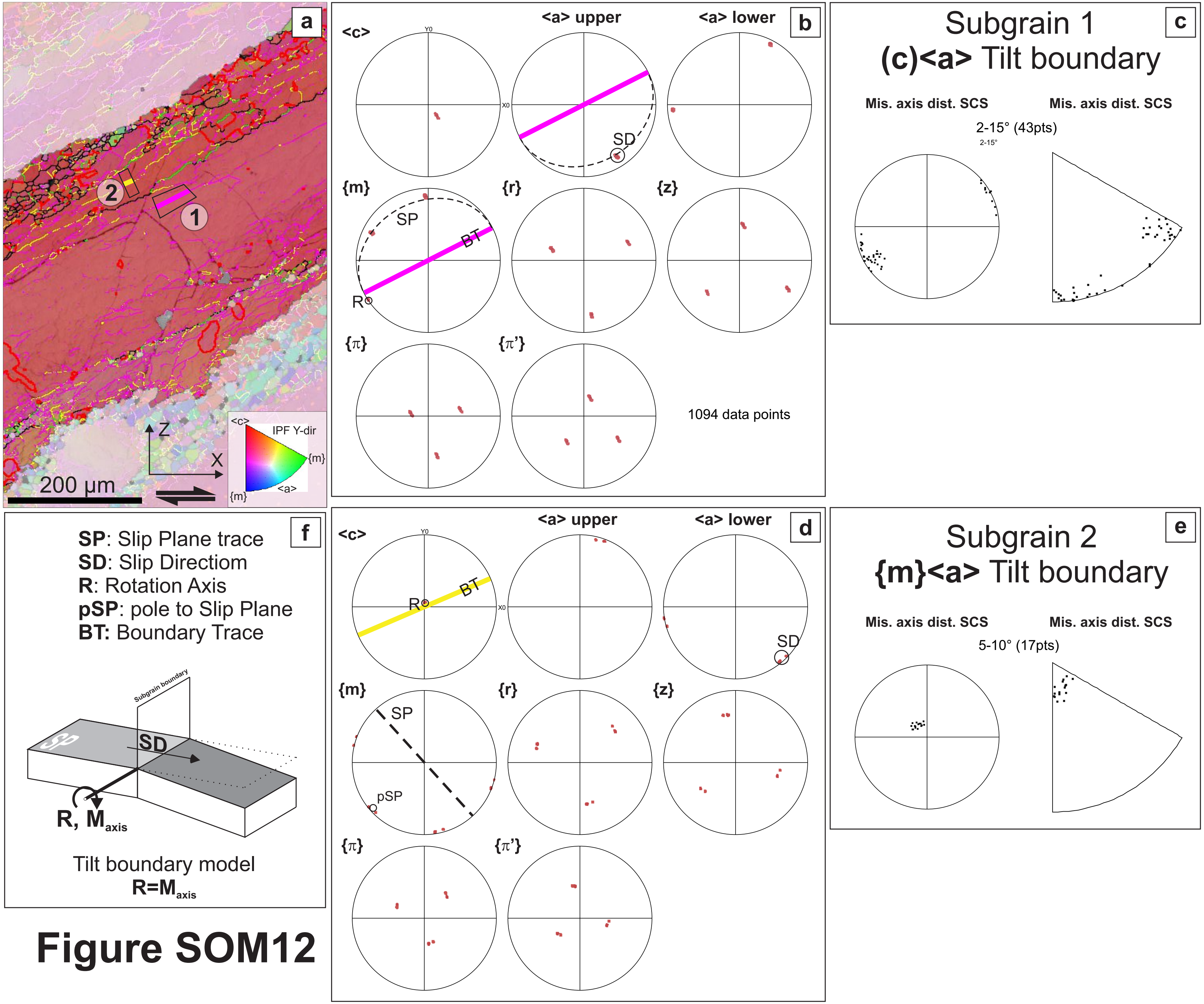

Figure SOM12

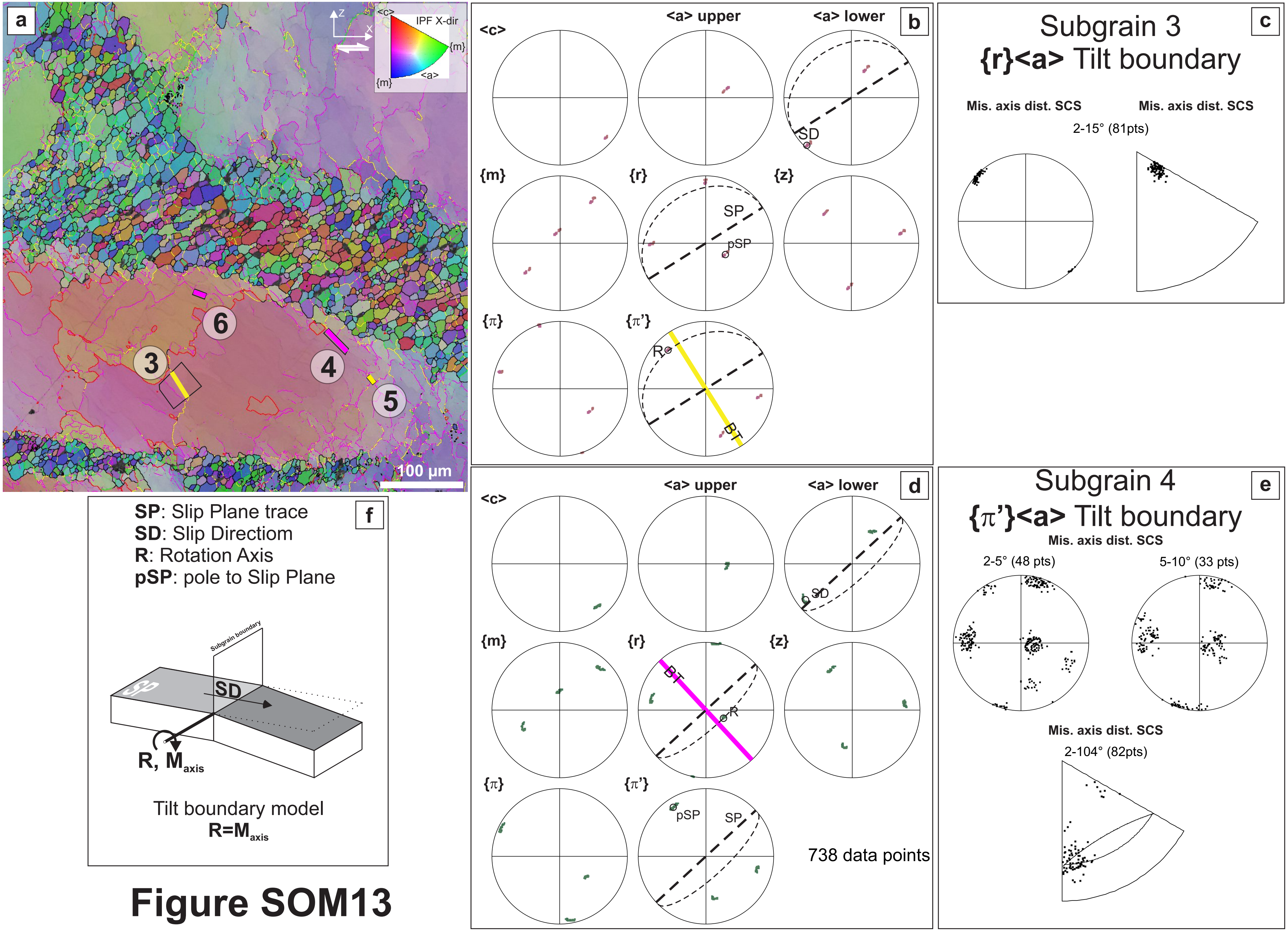

Figure SOM13

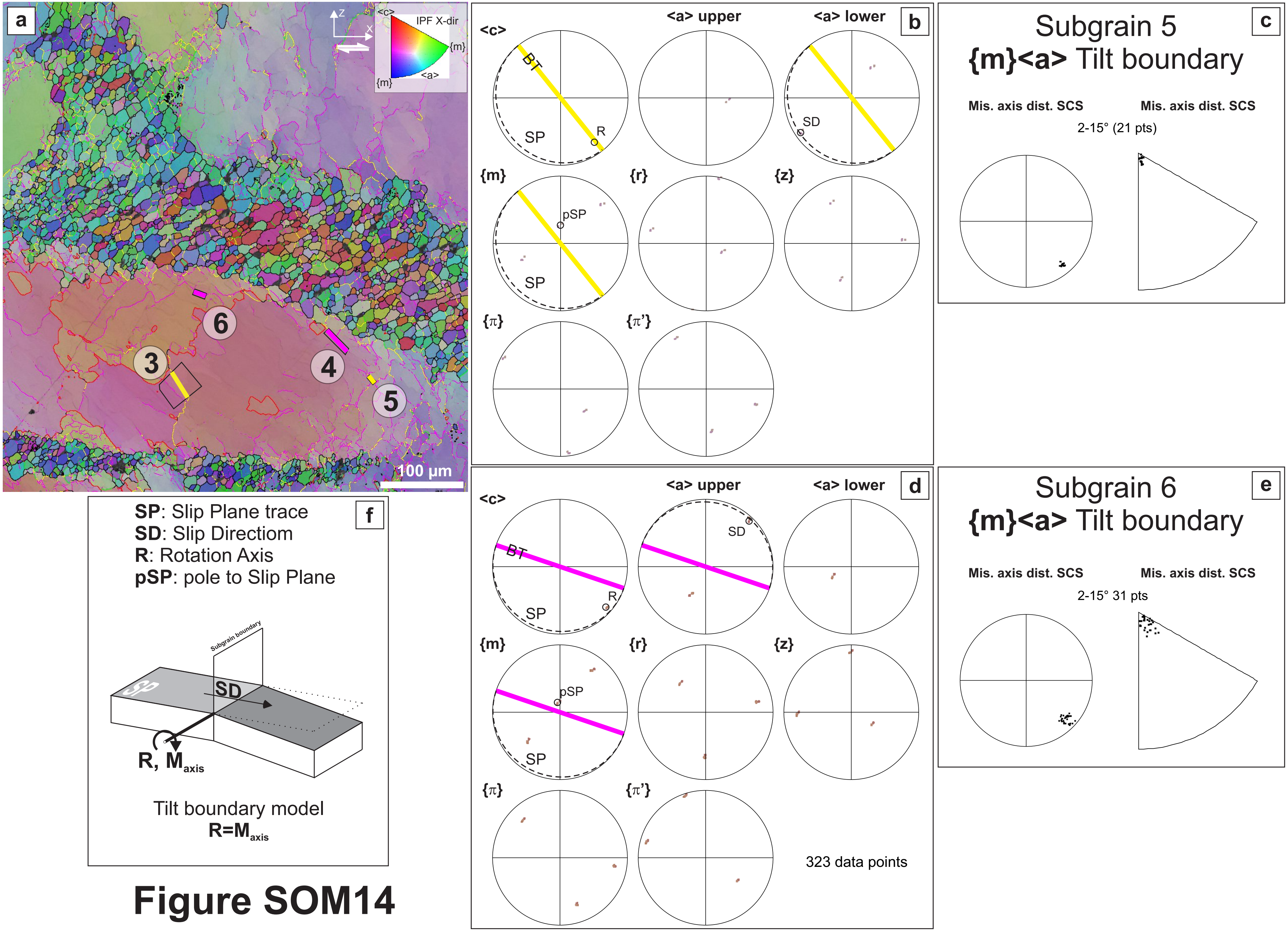

Figure SOM14

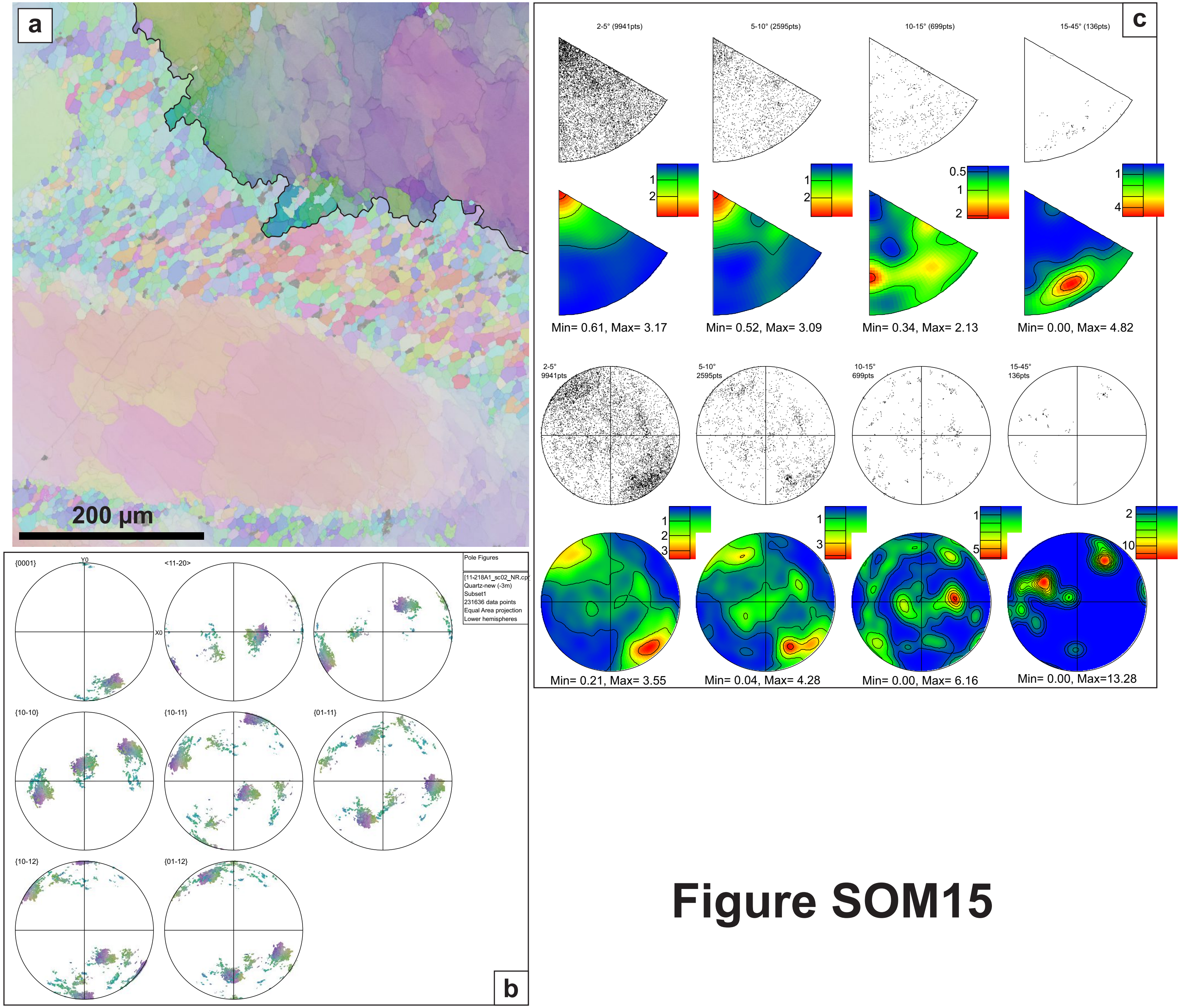

Figure SOM15

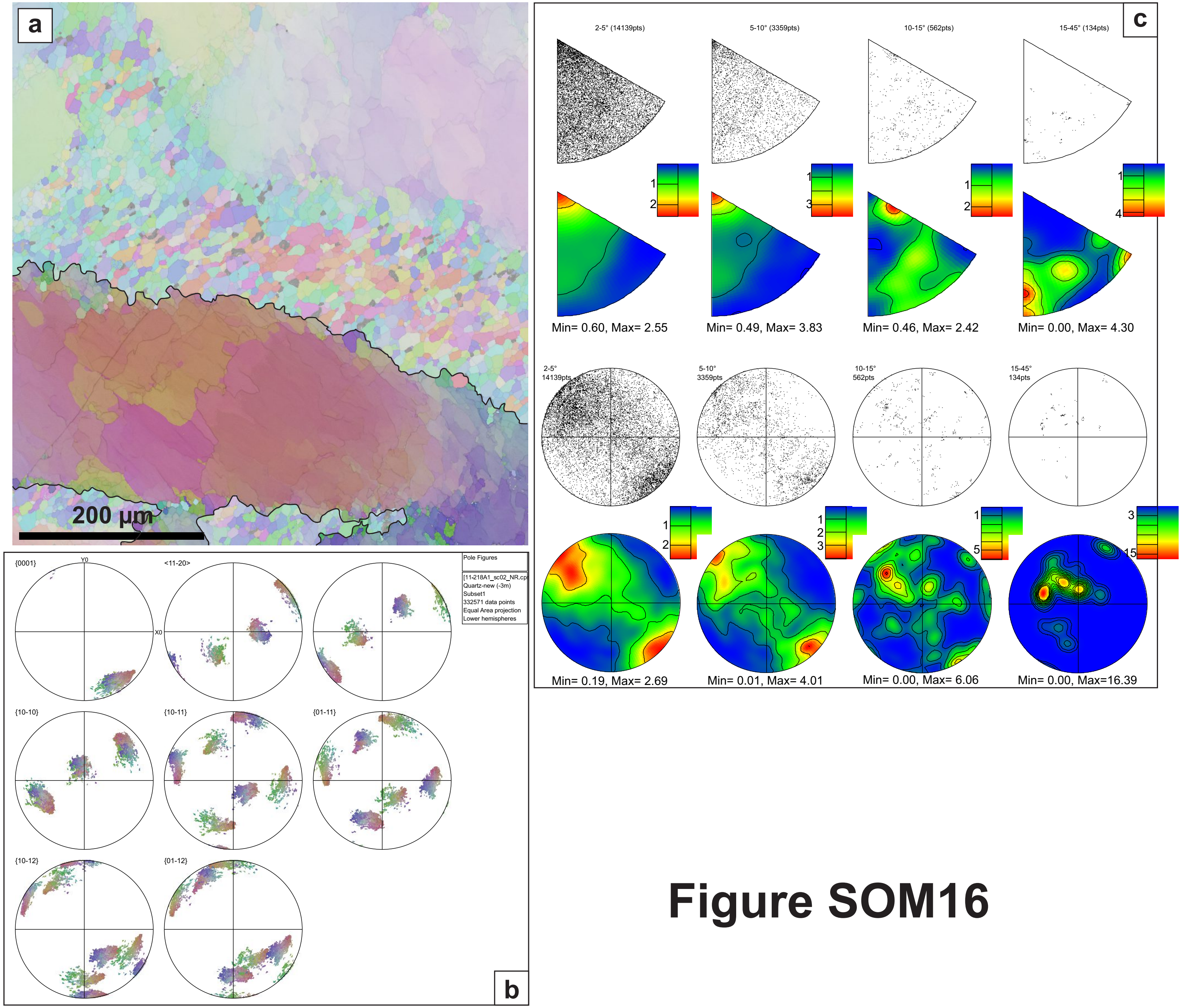

Figure SOM16

SEM-EBSD detector	FEG-SEM Zeiss 1540 EsB		JEOL 6610 LV SEM – NordLys Nano		JEOL 7001 FE SEM NordLys Max
Figure	Fig. 7	Fig. 8	Fig. 9	Fig. 6	Fig. 11
Subject	XZa-type μSZ	XZb-type μSZ	XZa-type μSZ	Y-type ribbon	Ultramylonite
Magnification	130x	120x	120x	120x	90x
Step size (μm)	0.6	0.6	1.8	1.2	1.6
Size (μm)	560 x 590	520 x 600	1076 x 806	1076 x 484	1422 x 1195
Acquisition time (s/pxl)	0.074	0.074	0.178	0.040	0.34
Accelerating Voltage	20	20	20	20	20

Table SOM1

Fig. SOM1: Microstructure and CPO of protomylonitic quartz vein. (a) Optical microphotograph (crossed polars and inserted gypsum plate) of the 2nd thin section used with that shown in Fig. 2a for the analysis of the protomylonite. (b) Sketch drawn from (a) showing the different ribbons (in different colours) and incipient recrystallization aggregates (in black colour). The ribbons are colour-coded as a function of the mean c-axis orientation determined from CIP analysis, accordingly with the Look-Up Table (LUT) reported in (d); (c) Analysis of the orientations of fine-grained recrystallized aggregates (in black colour) in selected ribbon portions of the protomylonite shown in (a). The orientations of the μSZ in the selected areas are shown in the rose diagrams. (d) CIP LUT showing (empty dots) the c-axis orientations of the ribbons. The dashed line represents the trace of the mylonitic foliation.

Fig. SOM2: Plot of the thickness versus displacement for μSZ within ribbon grains.

Fig. SOM3: Microstructures of sheared quartz veins. (a) Thick (mature) μSZ including small white mica flakes defining the internal oblique foliation. Note the extensive formation subgrains within the ribbon at the lower contact with the μSZ. Crossed polars. (b) Same as in (a) with crossed polars and inserted gypsum plate. (c) Partially recrystallized ribbons in a mylonite. Note the incipient formation of a lozenge-shaped ribbon leftover derived from a XZ-type ribbon (central part of the microphotograph). (d) Ribbons dissected by pervasive C'-type μSZs leading to formation quartz porphyroclasts in the ultramylonite. Crossed polars and inserted gypsum plate. (e) Ultramylonite showing extinction banding and including a ribbon leftover with an asymmetry unusual for a dextral sense of shear. Crossed polars. (f) Same as (f), but showing a more strongly asymmetric shape of the porphyroclast. (g) Secondary Electron (SE) SEM images of the grain surface of recrystallized grains along a μSZ in mylonites showing pores with a crystallographically-controlled regular geometric shapes (etch pit type). (h) Same as (g). Sense of shear is dextral in all (a)-(f) microphotographs.

Fig. SOM4: optical micrographs (crossed polarizers) of ribbon areas (highlighted by the red rectangle) selected for the EBSD analyses. (a) Y-type ribbon of Fig. 6. (b) XZa-type ribbon of Fig. 7. (c) XZb-type ribbon of Fig. 8. (d) Ultramylonite (recrystallized matrix and porphyroclasts) of Fig. 10. (e) XZa-type ribbon with mature μSZ of Fig. SOM5.

Fig. SOM5: EBSD orientation imaging and data for an XZa-type ribbon, and included mature μSZ ω−ψ−ξ, in the protomylonite. (a) Orientation map colour-coded according to the inverse pole figure shown in the lower right corner. Boundaries are colour-coded as a function of misorientations according to the same legend in Fig. 6a. (b) Pole figures for the host ribbon showing the orientations of [c], <a> and {r} crystallographic directions. The trace of the μSZ is shown as a red line. (c) Misorientation axis distributions for low (2-15°) and high (15-104°) misorientations in crystal and sample coordinates for the host ribbon. (d) Optical microphotographs (crossed polarizers) of the domain (included in the red box) shown in the EBSD map (a). (e) Pole figures ([c], <a> and {r} crystallographic directions) and misorientation axis distributions for low (2-15°), intermediate (15-45°) and high (45-104°) misorientations in IPF and sample coordinates for the μSZ domain ω. (f) Idem as (e) for the μSZ domain ξ. (g) Idem as (e) for the μSZ domain ψ. (h) Idem as (e) for the bulk μSZ (ω+ψ+ξ).

Fig. SOM6: Misorientation axis distributions for low (2-15°) and high (15-104°) misorientation in the host ribbons adjacent to incipient μSZ α (a) and β (b) of Fig. 8. Both (a) and (b) include the misorientation axes distribution in crystal coordinate (first row) and in samples coordinates (second row) in both raw and contoured format.

Fig. SOM7: Area-weighted grain size distributions (Herweg and Berger, 2004) for the recrystallized aggregates within μSZ zones: (a) incipient μSZ α (Fig. 8a); (b) evolved μSZ δ (Fig. 7a); (c-d) mature μSZ ε (Fig. 7a) and of Fig. 9a.

Fig. SOM8: Area-weighted subgrain size distributions (Herweg and Berger, 2004) for the host ribbon close to incipient μSZs α (a), β (b), and ϕ (c) of Fig. 8.

Fig. SOM9: Area-weighted grain size distributions (Herweg and Berger, 2004) for the recrystallized matrix aggregates of the ultramylonite of Fig. 11. (a) bulk ultramylonite (CPO in Fig. 11b); (b) recrystallized aggregate including the ribbon leftovers P (CPO in Fig. 10h); (c) layer I (CPO in Fig.10c); (d) layer II (CPO in Fig.10e); (e) layer IV (CPO in Fig.10f).

Fig. SOM10: Misorientation angle distribution for recrystallized aggregates of the ultramylonite of Fig. 10a. (a) bulk ultramylonite (CPO in Fig. 10b); (b) layer I (CPO in Fig.10c); (c) layer II (CPO in Fig.10d); (d) layer III (CPO in Fig.10e); (e) layer IV (CPO in Fig.10f); (f) ribbon leftover P (CPO in Fig.10g); (g) recrystallized aggregate around the ribbon leftovers P (CPO in Fig. 10h).

Fig. SOM11: Comparison between optical microstructure under crossed polarizers (right column) and SEM-CL images (left column). (a-b) Y-type ribbon. (c-d) Intersecting sets of recrystallized μSZs within a XZa-type ribbon; (e-f) Detail of a dextral μSZ within a XZa-type ribbon. (g-h) Ultramylonite showing a CPO banding and including a ribbon porphyroclast. Quartz luminescence is mainly related to the ~415 nm (blue) peak in panchromatic spectra that is strongly correlated with the trace concentration of Ti (Wark and Spear, 2005; Bestmann and Pennacchioni, 2015). Many studies have suggested that Ti resetting (and therefore resetting in CL patterns) in mylonitic rocks is enhanced by the occurrence of water-assisted deformation mechanisms and quartz precipitation (Grujic et al., 2011; Haertel et al., 2013; Bestmann and Pennacchioni, 2015). We performed a preliminary CL analysis of deformed Rieserferner quartz veins, with the purpose of detecting potential signatures for fluid-rock interaction during the different stages of shearing of the quartz veins.

We present CL images (Fig. SOM11) that provide evidence for the marked heterogeneity in the CL signal associated with the different microstructures. Protomylonites show complex and heterogeneous CL patterns (Fig. SOM11). The most strained parts of the XZ- and Z-type ribbons (that are less deformed than Y-type ribbons) have the lightest CL grey tones of the microstructure, which turn into dark tones in domains associated with crystal distortion, subgrain polygonization, incipient recrystallization and μSZs. The domains of homogeneous deformation of Y-type ribbons (Figs. SOM11a-b) show a pervasive regular array of bright CL linear features organized in 2 intersecting sets, forming a lozenge shaped grid, overprinting a dark grey CL background. In zones of distortion of the Y-type ribbons this array is dissected irregularly across a network of darker CL zones coinciding with aggregates of subgrains and new grains or highly distorted zones.

The dark CL zones of incipient recrystallization have a granular appearance that is more clearly shown at the higher magnifications in CL images of the µSZs across XZ-type grains (Figs. SOM11c-f). A direct comparison between the EBSD map of Fig. 7a and the corresponding CL image of Fig. SOM11f, clearly shows that the grains visible in the CL image perfectly match to subgrains and new grains along the µSZ. These grains visible in CL show a light grey core and a dark rim, which results in the grainy appearance of the zone of polygonization and recrystallization described above. Adjacent to µSZs there is commonly a very heterogeneous overprinting of the lighter CL tones of the less distorted portions of host ribbon by dark grey CL zones that are also associated with pervasive linear features subparallel to the main shortening direction. In general there is a coincidence between the CL darker tones with the most distorted parts of the ribbons. In ultramylonites, there is still heterogeneity in the CL patterns (Figs. SOM11g-h). The local ribbon leftovers have a lighter CL shade than the recrystallized matrix. This latter shows a CL banding, that partially matches the CPO banding, similar to that described by Bestmann and Pennacchioni (2015) for quartz in a mylonitic granodiorite.

Fig. SOM12: Boundary trace analysis (Prior et al., 2002; Piazolo et al., 2008) of the Y-type ribbon of Fig. 6a. (a) EBSD color-coded map with location of the analysed subgrain boundaries 1 and 2. (b) Pole figures (<c>, <a>, {m}, {r}, {z}, {π} and {π'} crystallographic orientations) for EBSD data points around subgrain boundary 1; (c) Misorientation axis in sample and crystal coordinates across subgrain boundary 1; (d) Pole figures for EBSD data points around subgrain boundary 2; (e) Misorientation axis in sample and crystal coordinates across subgrain boundary 2. (f) Scheme of relationships between tilt boundaries and edge dislocations. In the pole figure sets (b, d), the possible geometrical elements are shown for a tilt boundary due to the activity of (c) <a> slip (subgrain boundary 1) and {m}<a> slip (subgrain boundary 2).

Fig. SOM13: Boundary trace analysis (Prior et al., 2002; Piazolo et al., 2008) of the XZa-type ribbon of Fig. 7a. (a) EBSD color-coded map with location of the analysed subgrain boundaries 3-6. (b-e) Pole figures for subgrain boundary 3; (c) Misorientation axis in sample and crystal coordinates across subgrain boundary 3; (d) Pole figures for subgrain boundary 4; (e) Misorientation axis in sample and crystal coordinates across subgrain boundary 4. (f) Scheme of relationships between tilt boundaries and edge dislocations. In the pole figure sets (b, d), the possible geometrical elements are shown for a tilt boundary due to the activity of {r}<a> slip (subgrain boundary 3) and {π'}<a> slip (subgrain boundary 4).

Fig. SOM14: Boundary trace analysis (Prior et al., 2002; Piazolo et al., 2008) of the XZa-type ribbon of Fig. 7a. (a) EBSD color-coded map with location of the analysed subgrain boundaries 3-6. (b-e) Pole figures for subgrain boundary 5; (c) Misorientation axis in sample and crystal coordinates across subgrain boundary 5; (d) Pole figures for subgrain boundary 6; (e) Misorientation axis in sample and crystal coordinates across subgrain boundary 6. (f) Scheme of relationships between tilt boundaries and edge dislocations. In the pole figure sets (b, d), the possible geometrical elements are shown for a tilt boundary due to the activity of {m}<a> slip for both subgrain boundaries 5 and 6.

Fig. SOM15: Misorientation axis distribution for host ribbon of Fig. 7a (domain in the upper right side of the µSZ). (a) EBSD color-coded map (with semi-transparent colour for non-analysed areas). (b) Pole figures for <c>, <a>, {m}, {r}, {z}, {π} and {π'} crystallographic orientations. (c) Misorientation axis distribution diagrams (both inverse pole figures and in sample coordinates) for the misorientation ranges of 2-5°, 5-10°, 10-15° and 15-45°. See text for explanation.

Fig. SOM16: Misorientation axis distribution for host ribbon of Fig. 7a (domain in the lower left side of the μSZ). (a) EBSD color-coded map (with semi-transparent colour for non-analysed areas). (b) Pole figures for <c>, <a>, {m}, {r}, {z}, {π} and {π'} crystallographic orientations. (c) Misorientation axis distribution diagrams (both inverse pole figures and in sample coordinates) for the misorientation angle ranges of 2-5°, 5-10°, 10-15° and 15-45°. See text for explanation.

Table SOM1: Scanning electron microscope typology and analytical conditions for EBSD maps reported in Figs. 6-7-8, Fig. 10 and Fig. SOM5.

We present CL images (Fig. SOM15) that provide evidence for the marked heterogeneity in the CL signal associated with the different microstructures. Protomylonites show complex and heterogeneous CL patterns (Fig. SOM15). The most strained parts of the XZ- and Z-type ribbons (that are less deformed than Y-type ribbons) have the lightest CL grey tones of the microstructure, which turn into dark tones in domains associated with crystal distortion, subgrain polygonization, incipient recrystallization and μSZs. The domains of homogeneous deformation of Y-type ribbons (Figs. SOM15a-b) show a pervasive regular array of bright CL linear features organized in 2 intersecting sets, forming a lozenge shaped grid, overprinting a dark grey CL background. In zones of distortion of the Y-type ribbons this array is dissected irregularly across a network of darker CL zones coinciding with aggregates of subgrains and new grains or highly distorted zones. The dark CL zones of incipient recrystallization have a granular appearance that is more clearly shown at the higher magnifications in CL images of the μSZs across XZ-type grains (Figs. SOM15c-f). A direct comparison between the EBSD map of Fig. 7a and the corresponding CL image of Fig. SOM15f, clearly shows that the grains visible in the CL image perfectly match to subgrains and new grains along the μSZ. These grains visible in CL show a light grey core and a dark rim, which results in the grainy appearance of the zone of polygonization and recrystallization described above. Adjacent to μSZs there is commonly a very heterogeneous overprinting of the lighter CL tones of the less distorted portions of host ribbon by dark grey CL zones that are also associated with pervasive linear features subparallel to the main shortening direction. In general there is a coincidence between the CL darker tones with the most distorted parts of the ribbons. In ultramylonites, there is still heterogeneity in the CL patterns (Figs. SOM15g-h). The local ribbon leftovers have a lighter CL shade than the recrystallized matrix. This latter shows a CL banding, that partially matches the CPO banding, similar to that described by Bestmann and Pennacchioni (2015) for quartz in a mylonitic granodiorite.

Table SOM1: Scanning electron microscope typology and analytical conditions for EBSD maps reported in Figs. 6-9 and Fig. 11.